INFRARED AND PASSIVE MICROWAVE

SATELLITE RAINFALL ESTIMATE

OVER TROPICS

_____

A Thesis Presented to the Faculty of the Graduate School

University of Missouri - Columbia

_____

In Partial Fulfillment

Of the Requirement for the Degree

Master of Science

_____

by

BUN LIONG SAW

Dr. Neil I. Fox, Thesis Supervisor

DECEMBER 2005

For

My Parents

My Wife, Shor Khing

My Children, Shirley, Vincent and Sharmin

Life's battles don't always go,

To the *stronger* or *faster* man,

But *soon* or *late* the man who *wins*,

Is the man **WHO THINKS HE CAN!**

-   *Anonymous*

COMMITTEE IN CHARGE OF CANDIDACY

Assistant Professor Dr. Neil I. Fox
<u>Chairperson and Advisor</u>

Associate Professor Dr Anthony R. Lupo

Associate Professor Dr Chris K. Wikle

Adjunct Professor Emeritus Ronald E. Rinehart

Acknowledgements

Not forgetting my great appreciation goes my parents for their support, my wife, Shor Khing for her patience and understanding allowing me taking a lot of time away to prepare for this thesis and my three wonderful kids, Shirley, Vincent and Sharmin for their presence here that made this place far away from home just like back home in our country. It is a shear joy to see them grow and discover new experiences in their life. They are the source of my inspiration and strength in my continuous endeavors.

Last, but by no means least, I would like to Malaysian Government through Public Service Department for giving me and my family the financial support needed for the completion of my studies.

Once against to all of you, **THANK YOU** from the bottom of my heart!!!

Table of Contents

List of Figures

List of Tables

Abstract

Precipitation is an important but highly variable atmospheric parameter. Existing rain gauge networks cannot provide the temporal and spatial coverage that is needed to monitor it sufficiently. Weather radars are directly sensitive to precipitation elements, and hence are valuable tools in precipitation observation. However, their application for accurate precipitation estimation with good spatial coverage is hampered by the existing gaps in radar networks, and by technical problems. Satellite measurements have the advantage of providing spatially homogenous observations over large areas.

Peninsular Malaysia is bounded by latitudes 0 - 8°N and longitude 100 -105°E. During the Northern Winter Monsoon period, the east coast of the peninsula is affected by torrential monsoon rain. The monthly average rainfall of more than 650 mm more often than not causes flooding, and affects the livelihood of more than five million people living there.

This study was conducted to evaluate the performance of the combined infrared and microwave algorithm (MWL) rainrate estimation compared to rain gauge values over the tropical region. The combination of the Kurino (1997) Look-Up Table (LUT) Method and the Advanced Microwave Sounding Unit

(AMSU) rainrate algorithm used by National Environmental Satellite Data and Information Service (NESDIS) were used for this study. This is the latest passive microwave algorithm; it is highly correlated with the surface rain rates and is now directly used to monitor surface precipitation throughout the world (Weng *et al.*, 2003).

The results indicated that, generally, the MWL performed better than that of LUT estimate. The correlation coefficients of the MWL and LUT varied from 0.70 to 0.81 as compared to rain gauge values. The slope of the MWL regression line to the rain gauges is 0.86 that of LUT is 0.47.

Despite the improvements, there are many difficulties and challenges in satellite rainfall estimation. The nature of rainfall, the temporal and spatial resolution of satellite observations, the time lag between satellite and ground observations are some factors that have a significant impact on the results of the study.

Chapter 1 Introduction

Water is one of the most universal minerals in the world, and the most vital for human life and activity. Unfortunately, its availability to man is restricted by factors of local supply, natural purity, and its unique ability to be present in gaseous, liquid, and solid forms within the common range of environmental conditions found at or near the surface of the Earth. The source of all water in its most desirable state is precipitation, whose natural purity is generally high. It is not surprising that so much time and effort has been and is being spent in the evaluation of rainfall through both time and space (Barrett and Martin, 1981).

Precipitation is an important but highly variable atmospheric parameter. The existing rain gauge networks cannot provide the temporal and spatial coverage that is needed for its sufficient monitoring. Weather radars are directly sensitive to precipitation elements and hence are valuable tools in precipitation observation. However, their application for accurate precipitation estimation with good spatial coverage is hampered by gaps in radar networks, and by technical problems (absorption of the radar signal in precipitation elements, calibration difficulties, the formation or evaporation of precipitation below the radar beam, etc.). Satellite measurements have the advantage of providing spatially homogenous observations over large areas. Over the past three decades there have been numerous attempts to use satellite measurements for precipitation

estimation. So far, mainly passive visible, infrared or microwave measurements from the geostationary or polar orbiting meteorological satellites have been used for this purpose. Visible and infrared satellite measurements, however, observe only the cloud top and are not sensitive to the physical characteristics of clouds, and hence provide only indirect information on precipitation. In addition, the temporal resolution of satellite measurements is generally worse than that of radar observations. There is no doubt that the most accurate estimates can be expected from the synergistic use of multispectral satellite and radar information wherever it is possible.

This study is concerned with the area of Peninsular Malaysia bounded by latitudes 0° - 8°N and longitudes 100° -105°E. During the Northern Winter Monsoon period; the east coast of the peninsula is affected by torrential monsoon rain. A monthly average rainfall of more that 650 mm, more often than not, causes flooding over the area. This annual phenomenon affects the livelihood of more than five million people living there.

It is worthwhile to briefly describe synoptic weather situations over the study region because cloud formation is closely associated with the large-scale synoptic environment. The weather in Malaysia is characterized by two monsoon regimes, namely, the Summer Monsoon from late May to September, and the Winter Monsoon from November to March. The Winter Monsoon brings heavy rainfall with the march of the Intertropical convergence zone (ITCZ) through Malaysia, particularly to the east coast states of Peninsular Malaysia, whereas the Summer Monsoon normally signifies relatively drier weather. The transition

period in between the monsoons is known as the intermonsoon period.

The Winter Monsoon in Malaysia, characterized by steady northeast trade winds usually occurs from mid-November till early March. During this period, the east coast states of Peninsular Malaysia will experience widespread heavy rain spells of 2 to 3 days duration. About 3 to 4 such heavy rain spells are expected to occur over the above areas at different times throughout the Winter Monsoon season. Between these heavy rain spells, the weather is either relatively fair or with little rain. In the months November and December, the west coast states of Peninsular Malaysia will frequently experience thunderstorms in the afternoon and night.

The monsoon rains over Kelantan and Terengganu (the north eastern states) usually begin after mid-November. Pahang and east Johore (eastern states) usually receive heavy rainfall in December and early January. Figure 1.1 shows states in Peninsular Malaysia and mean monthly rainfall for December. During the months of November and December, the widespread continuous rain that occurs over the east coast states might spill over to the west coast states which will bring continuous widespread rain lasting for a few hours. From mid-January the weather begins to be relatively drier over Peninsular Malaysia. Thus, the likely occurring cloud types during the analysis period consist of a mixture of precipitating convective and stratiform clouds.
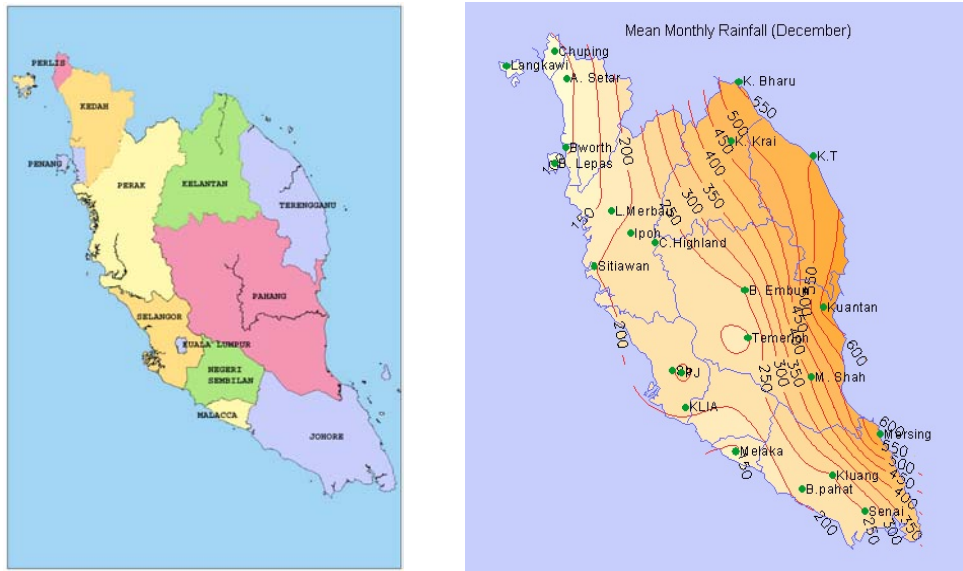
(a)   States in the Peninsula   (b)   December Mean Monthly Rainfall

Figure 1.1   Peninsular Malaysia map (a) States in the Peninsula
and (b) Mean monthly rainfall for December

In this study, activities related to precipitation estimation are based on GMS-5 and GOES-9 geostationary satellite data obtained from the ASEAN Special Meteorological Center (ASMC), Advanced Microwave Sounding Unit (ASMU) onboard NOAA polar orbiting satellite from NOAA/NESDIS and rain gauge data from Malaysian Meteorological Service (MMS).

1.1   Statement of Thesis

The purpose of this study is to examine the performance of the combined satellite rainfall estimation Infrared (IR) technique and the latest Passive Microwave (PMW) algorithm. Retrieved rain rates will be compared with that of the ground-based rain gauge observation networks maintained by the Malaysian Meteorological Service (MMS). This is an attempt to take advantage of the higher temporal resolution of GMS observations and a more physically direct rainfall measurement of microwave technique. The PMW algorithm used in this study is the latest from NOAA NESDIS, it is highly correlated to with the surface rain rates and is now directly used to monitor surface precipitation throughout the world (Weng *et al.*, 2003).

1.2   Objectives

The objectives of this study are

(i)   To evaluate the performance of satellite rainfall estimate using IR technique as compared to ground-based rain gauges observations,

(ii)   To determine the relationship function of the PMW rainrate and IR technique,

(iii)   To evaluate the performance of the combined satellite rainrate estimation technique.

Chapter 2   Background

2.1   Meteorological Satellites

On April 1, 1960, the world's first meteorological satellite (metsat), TIROS-1 (Television and Infra-Red Observation Satellite) was launched by the United States (e.g., Rao, *et al.*, 1990). Nine additional satellites were launched in the TIROS series; the last, TIROS 10, was launched on July 2, 1965.

In 1964, an extremely important series of experimental satellites was initiated, the Nimbus series. Nimbus 1 was launched August 28, 1964. It was the first sunsynchronous satellite, which means that it passed over any point on Earth at approximately the same time each day and it also was the first three-axis stabilized metsat. In total, seven Nimbus satellites were launched; the last one, Nimbus 7, was launched on October 24, 1978.

By 1966, the United States was ready to initiate an operational series of metsats. The Environmental Science Service Administration (ESSA: NOAA's predecessor) commissioned nine satellites, ESSA 1 through 9, which were launched between February 3, 1966 and February 26, 1969. The second series of U.S. operational metsats began on January 23, 1970 with the launch of TIROS M, also known as Improved TIROS Operational System (ITOS). The NOAA 1 through 5 satellites completed the series. NOAA 5 was launched on July 29,

1976. The third generation of U.S. polar-orbiting metsats began on October 13, 1978 with the launched of TIROS N series (NOAA 6 through 14). The current polar-orbiting series, the NOAA KLM, are the modified versions of TIROS N and are called Advanced TIROS N (ATN) with additional instruments onboard that are not directly related to meteorology such as Search and Rescue system.

Other series of polar-orbiting metsats are the Defense Meteorological Satellite Program (DMSP) operated by the U.S. Department of Defense (DoD), METOP operated by European Organization for the Exploitation of Meteorological Satellites (EUMETSAT), Feng Yun-1/3 (FY-1/3) operated by China and METEOR operated by Russia.

The first generation semioperational geostationary metsats began with the launch of the Synchronous Meteorological Satellite 1 (SMS 1) on May 17, 1974 followed by SMS 2 on Feb 6, 1975. The first truly operational geostationary metsat, the Geostationary Operational Environmental Satellite 1 (GOES 1), was launched on October 16, 1975. GOES 2 and 3 were similar. Since the launch of SMS 2, the United States has generally maintained two geostationary satellites in orbit one at longitude 75º west, and one at 135º west.

On September 9, 1980, GOES 4, the first in the second generation of GOES satellites, was launched followed by GOES 5 through 7. The current generation of GOES satellites constitutes five satellites, namely GOES 8 through 12. GOES 8 was launched on April 13, 1994 (Kidder and Vonder Haar, 1995).

Other geostationary metsats are Meteosat/MSG, stationed at the prime meridian operated by EUMETSAT, GOMS/Electro at 76º east operated by Russia, INSAT at 83º east operated by India, FY 2/4 at 105º east operated by China and GMS/MTSAT at 140º east operated by Japan.

Nowadays, there are two types of meteorological satellites in operation, namely, geostationary satellites and polar orbiting satellites. Figure 2.1 shows the locations of geostationary, polar-orbiting metsats and research satellites.
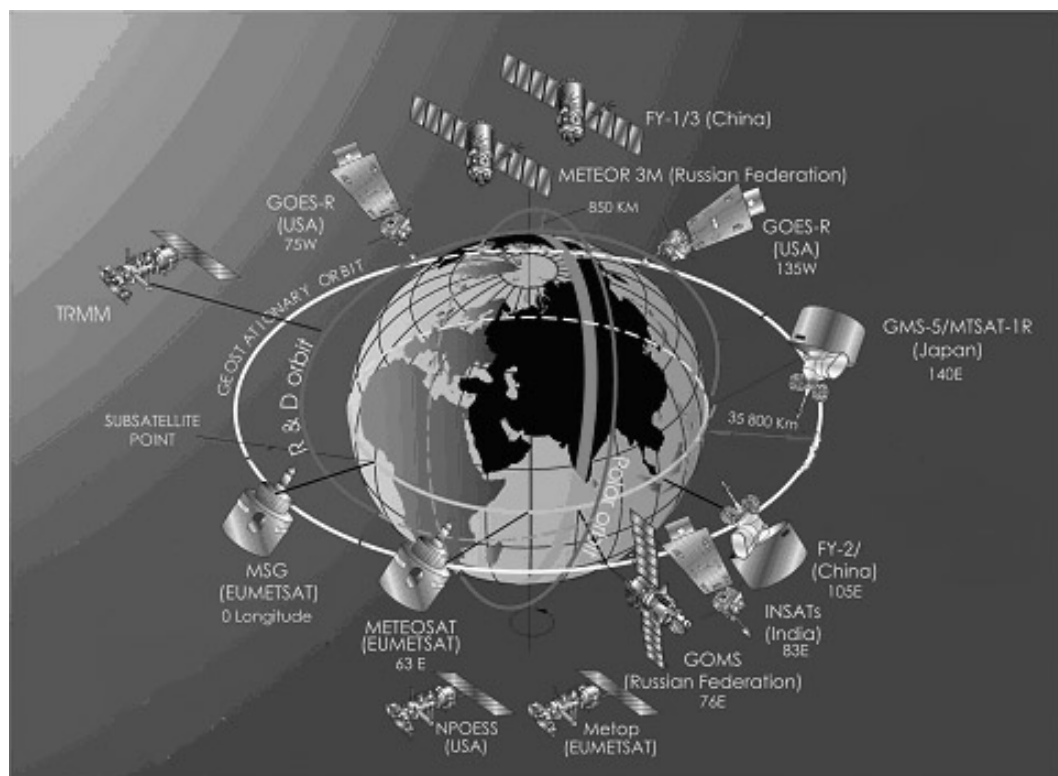
Figure 2.1   Global networks of Geostationary and Polar-Orbiting satellites (http://www.wmo.int/index-en.html space-based global observation systems)

2.1.1   Operational Geostationary Satellites

The operational geostationary satellites orbit around the Earth at an altitude of about 35 800 km above the equator, as shown in Fig. 2.1. At this height, the angular velocity of the spacecraft is equal to the angular velocity of the Earth (each travels 360°, or one complete orbit, in 24 hours). As a result, each satellite remains over the same point of the Earth throughout its entire orbit.

The main advantage of geostationary satellites lies in the high temporal resolution of their data. A fresh image of the whole Earth is available every 30 mins. On some geostationary satellites, the scanning mode can be altered to observe a small selected area even more frequently.

The main disadvantage of many geostationary satellites is their limited spatial resolution, which is a consequence of their distance from the Earth. Technical advances will bring improvements in this respect, but will not reduce the distortion of imagery in high latitudes, which is the result of viewing the Earth at an increasingly oblique angle. Useful information is restricted to the belt between 60° N and 60° S (Bader, *et al.*, 1995). Figure 2.2 shows the global coverage of geostationary metsats.
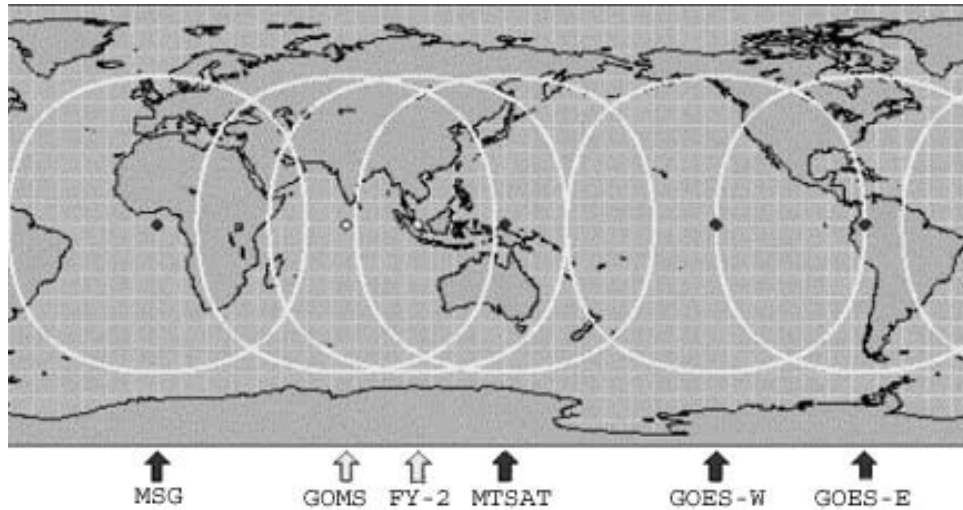
Figure 2.2   Geostationary meteorological satellite coverage
(from http://www.wmo.int/index-en.html).

2.1.2   Operational Polar Orbiting Satellites

The orbits of the polar orbiting satellites are nearly from pole to pole at the height of about 860 km, as shown in Fig. 2.1. Polar orbiting satellites circle the Earth in a sun synchronous orbit: the orbital plane of a polar orbiting satellite remains stationary with respect to the sun. As the satellite moves through its orbit, the Earth rotates below it. The result is that the satellite scans a different strip of the Earth during each orbit (swath).

From a fixed point on Earth, a polar orbiting satellite will always cross the equator at approximately the same local time relative to the sun. Each orbit has a period of approximately 102 mins. The swaths are usually about 2 600 km wide and, by completing 14 orbits per day, one satellite can provide a complete coverage of the globe twice every 24 hours (Conway, 1997). Figure 2.3 shows the coverage for polar-orbiting metsats.
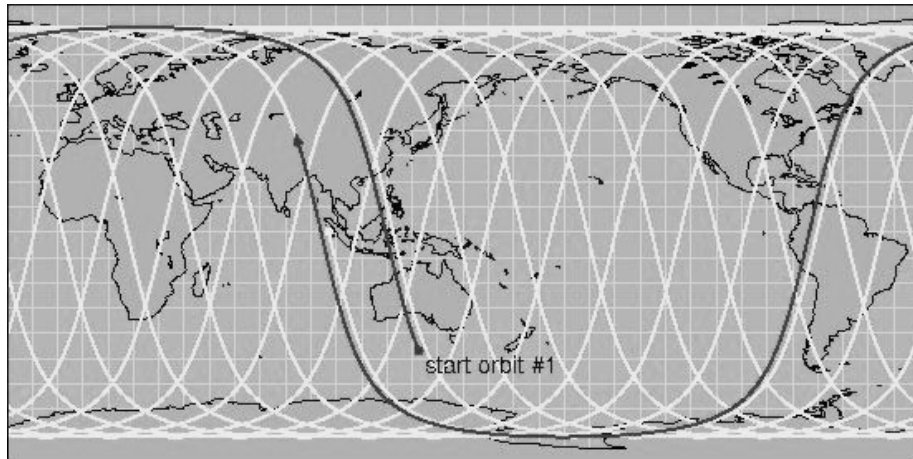
Figure 2.3   Polar-Orbiting satellite coverage
(from http://www.wmo.int/index-en.html).

2.2   Radiation, the Atmosphere and Satellite Sensors

All the information received by a satellite about the Earth and its atmosphere comes in the form of electromagnetic radiation. It is necessary, therefore, to understand the mechanisms by which this radiation is generated and how it interacts with the atmosphere.

Electromagnetic radiation consists of alternating electric and magnetic fields (Fig. 2.4). The electric field vector is perpendicular to the magnetic field vector, and the direction of propagation is perpendicular to both. Radiation is often specified by its *wavelength (λ),* which is the distance between crests of electric or magnetic field.
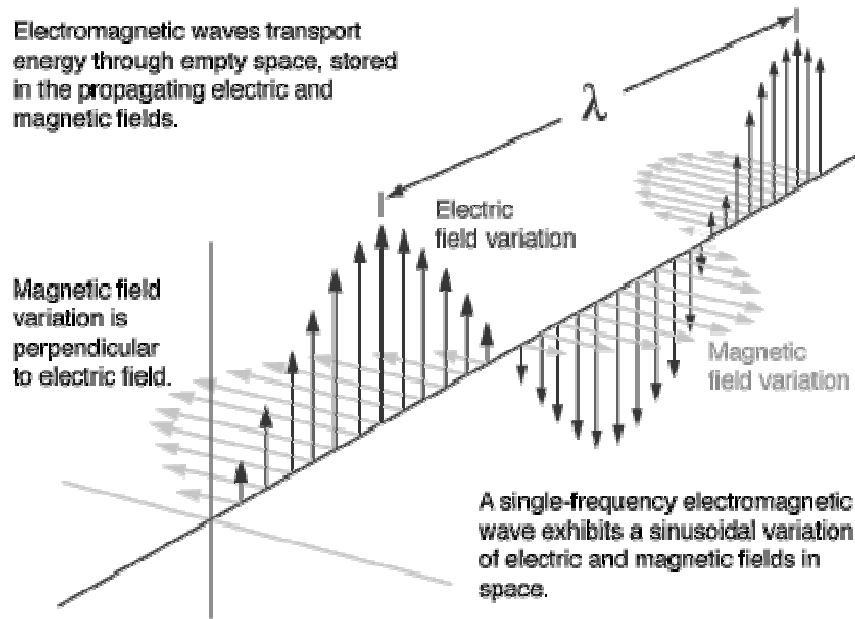
Figure 2.4   Schematic representations of electromagnetic waves
(from http://micro.magnet.fsu.edu).

Figure 2.5 shows the electromagnetic spectrum. A broad range of wavelengths, including the ultraviolet to microwave region, is useful in satellite meteorology.
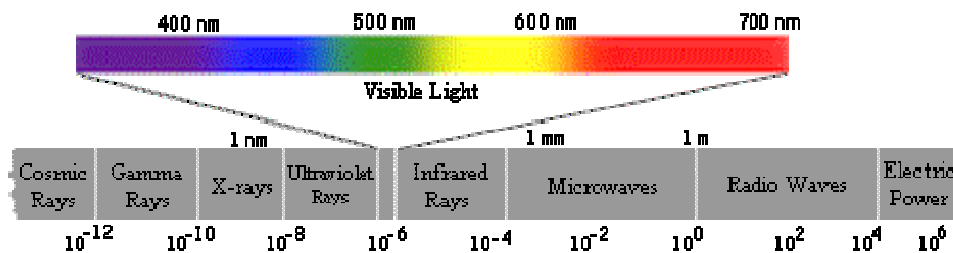
Figure 2.5   Electromagnetic spectrum

The *frequency (f)* is related to the *wavelength (λ)* by

$$f \quad = \quad c \, / \, \lambda, \tag{2.1}$$

where *c* is the speed at which electromagnetic radiation travels and is known as the *speed of light*. In vacuum the speed of light is 2.9979×10^8 m/s. In the atmosphere, it travels slightly more slowly, due to interaction with air molecules.

The *index of refraction n* of a substance is the ratio of speed of light in vacuum to the speed at which electromagnetic radiation travels in that substance. At sea level, the index of refraction of air is approximately 1.0003. Strong vertical gradients of atmospheric density and humidity result in strong vertical gradients of *n*. These cause bending of electromagnetic rays and can cause slight mislocation of satellite scan spots.

2.2.1 Blackbody Radiation

All material above absolute zero in temperature emits radiation. A perfect emitter, known as a *blackbody* emits the maximum amount of radiation. No real material is a perfect blackbody, although some materials come very close to being perfect emitters in some wavelength ranges. The blackbody radiation depends on two variables, temperature and wavelength.

The radiation by a blackbody is given by the *Planck function*,

$$B_\lambda(T) = \frac{2hc^2\lambda^{-5}}{\exp\left(\dfrac{hc}{\lambda kT}\right) - 1} \tag{2.2}$$

where B_λ is the radiance at wavelength λ, and absolute temperature T, c is the speed of light, h is Planck's constant (6.6261×10^{-34} J s) and k is Boltzmann's constant (1.3807×10^{-23} J K^{-1}). The Planck function is more conveniently written as

$$B_\lambda(T) = \frac{c_1\lambda^{-5}}{\exp\left(\dfrac{c_2}{\lambda T}\right) - 1} \tag{2.3}$$

where $c_1 = 2hc^2$ (1.1910×10^{-16} W m^2 sr^{-1}) and $c_2 = hc/k$ (1.4388×10^{-2} m K), which are the first and second radiation constants, respectively. Figure 2.6 shows B_λ plotted against wavelength (Kidder and Vonder Haar, 1995).
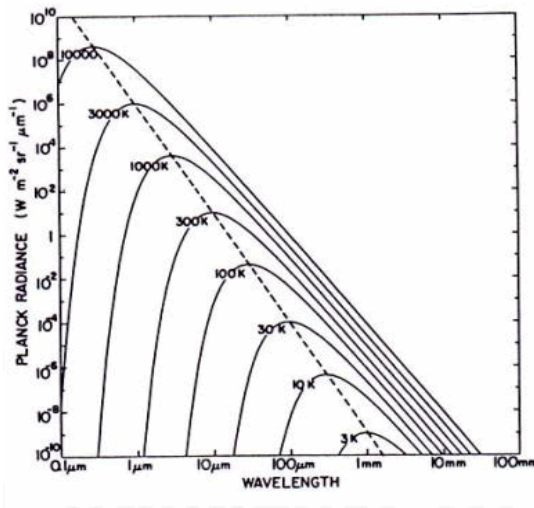
Figure 2.6   Planck radiations versus wavelength for the indicated temperature.

14

The emittance of real materials is enormously variable. Figure 2.7 shows the normalized Planck curves representing solar radiation (5780 K) and terrestrial radiation (255 K).
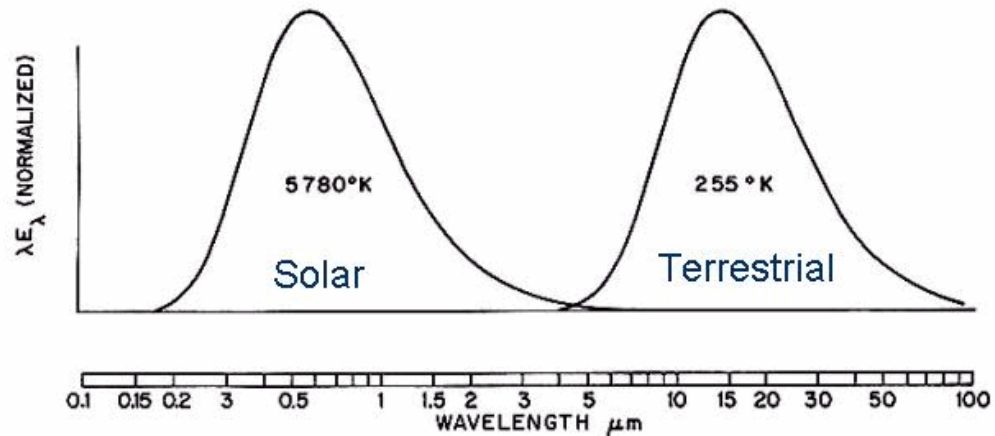
Figure 2.7   Emittance as a function of wavelength for two materials used in a satellite radiometer. (from Wallace and Hobbs, 1977)

Typical earth atmospheric temperatures (which include the clouds), in the range 200 – 300 K, emit peak radiation in the wavelength range of 7.5 – 14.5 µm. While the sun with the surface temperature of approximately 6000 K, has its maximum emission at a wavelength of 0.48 µm. These results can be obtained using the *Wien's Displacement Law*;

$$\lambda_m T \quad = \quad 2897.9 \; \mu m \; K, \tag{2.4}$$

where λ_m is the wavelength of maximum emission for a blackbody at temperature, T. The peak wavelength ranges for the Earth and Sun respectively correspond to the infrared waveband and visible band, respectively, sensed by the satellite radiometer.

The total radiant flux (energy) from the cloud top is given by *Stefan-Boltzmann equation*,

$$F_{BB} = \int_0^\infty \pi B_\lambda(T) d\lambda = \frac{\pi^5}{15} c_1 c_2^{-4} T^4 = \sigma T^4 \tag{2.5}$$

where σ is the Stefan-Boltzmann constant (5.67×10^{-8} W m^{-2} K^{-4}). For objects other than ideal blackbodies,

$$F_{BB} \quad = \quad \varepsilon \, \sigma \, T^4 \tag{2.6}$$

where ε is the emissivity of the object ($\varepsilon = 1$, for a blackbody). The emissivity lies in the range $0 < \varepsilon < 1$ depends on the type of material and temperature of the surface.

Solid angle, ω, is a measure of how much satellite field of view is occupied by an object (the cloud in this case). The solid angle subtended by the cloud to the satellite radiometer is given by

$$\omega = (\pi R^2 / 4\pi D^2) \times 4\pi \qquad (2.7)$$

where R is the radius of the cloud and D is the distance of the cloud top to the satellite.

To measure the brightness temperature (TB) we need to calculate the amount of energy received by the satellite sensor and, by inverting Planck's equation, TB at a given wavelength can be obtained as follows,

$$TB = \frac{c_2}{\lambda \ln\left(\dfrac{c_1 \lambda^{-5}}{B_\lambda(T)} + 1\right)} \qquad (2.8)$$

where c_1 and c_2 are constants from Planck's equation (2.3) and λ is the central wavelength of the IR channel (in μm). From TB, the height of cloud top can be inferred from upper air observations.

For microwave remote sensing the wavelengths are quite long, $\lambda \sim 1$ mm or longer, and for the temperatures encountered on Earth and in its atmosphere, $c_2 / \lambda T \ll 1$. Thus, $\exp(c_2 / \lambda T)$ in equation 2.3 can be approximated by $1 + c_2 / \lambda T$. TB then becomes

$$TB = \frac{B_\lambda(T)}{\dfrac{c_1}{c_2} \lambda^{-4}} \qquad (2.9)$$

This is known as the *Rayleigh-Jeans approximation*. It says that in the microwave portion of the spectrum, brightness temperature is simply proportional to radiance.

2.2.2   Atmospheric Windows

Most remote sensing is conducted above the Earth either within or above the atmosphere. The gases in the atmosphere interact with solar radiation and with radiation from the Earth's surface. Although the incoming radiation is a single source of excitation of atoms and molecules in the air and any materials found at the surface, that electromagnetic radiation will experience varying degrees of transmission, absorption, emittance, and/or scattering, depending on whatever wavelengths are considered. Figure 2.8 shows the "fate" of the radiation in the atmosphere.
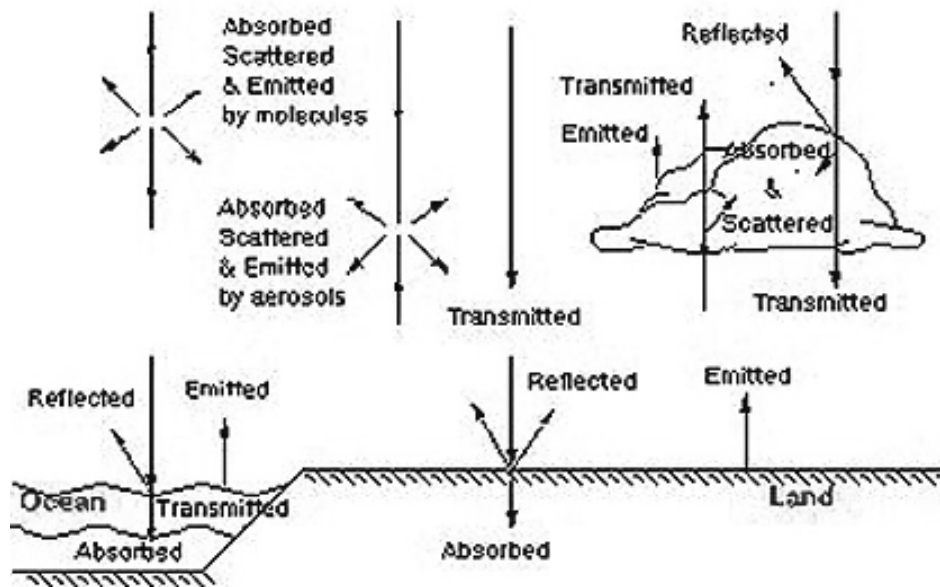
Figure 2.8   Atmospheric radiation processes
(from http://rst.gsfc.nasa.gov).

At some wavelengths the atmosphere is partly to completely transparent; at others, photons are variably absorbed by interaction with air molecules. Figure 2.9 shows relative atmospheric radiation transmission and absorption at different wavelengths.
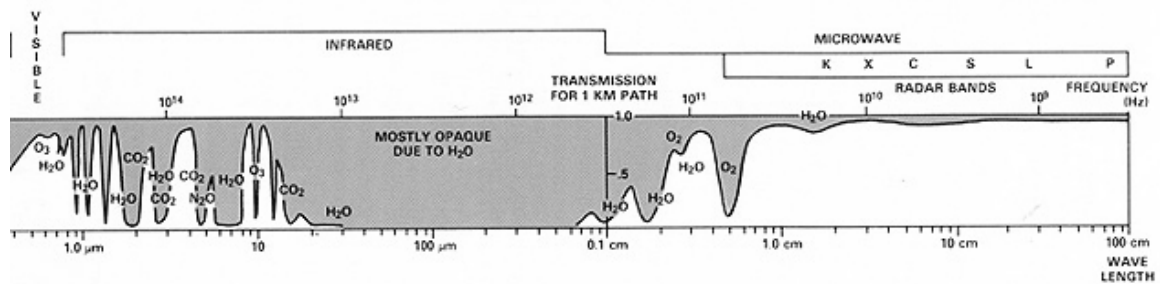
Figure 2.9   Relative atmospheric radiation transmissions and absorption
at different wavelengths (from http://rst.gsfc.nasa.gov).

Shaded zones mark minimal passage of incoming and/or outgoing radiation, whereas white areas denote atmospheric windows, in which the radiation does not interact much with air molecules and hence, is not absorbed.

2.3 The Satellite Rainfall Estimation Techniques

The advent of geostationary metsats has provided a new perspective in meteorology by world-wide observation of weather phenomena from space. Since remote areas not covered with conventional observation networks can now be continuously monitored, geostationary weather satellites have become an essential component of short-term weather monitoring and forecasting. In particular, there has been great emphasis in recent decades on monitoring rainfall from time-lapsed geostationary satellite imagery in the context of weather and flood forecasting. As a result, there is a history of literature on rain retrieval in both the infrared and microwave spectrums dating back to the 1970s.

Infrared radiation measurements from geostationary satellites have been widely used for rain estimation in spite of an inherent weakness of the physical relation between cloud top temperature and underlying rainrate. Yet, time-sequenced imagery provides an excellent depiction of the movement of clouds and weather systems.

Microwave measurements from passive sensors aboard low Earth-orbiting metsats have more direct and physical connections, since microwave frequencies respond directly to atmospheric hydrometeors through scattering and emission processes. Nevertheless, the broader spatial resolution and less frequent temporal coverage of microwave sensors hinders a direct application to weather forecasting, especially associated with rapidly developing severe storms.

Currently, geostationary metsat data are the only means to provide cloud information at near-continuous space and time scales necessary for both weather forecasting and nowcasting in many regions. This is particularly true when monitoring storm development associated with heavy rain events accompanied by meteorological phenomena such as typhoons and monsoon fronts over the South China Sea, because of the high spatial and temporal variability associated with these storms.

Various rain estimation algorithms have been developed using geostationary satellite data (e.g., Barrett, 1970 and 1973; Scofield and Oliver, 1977; Arkin, 1979; Negri *et al*, 1984; Adler and Negri, 1988; Kurino, 1997; Grose *et al*, 2002). However, direct application of these published IR-based algorithms to the tropical weather phenomena has remained elusive because they were developed under specific climatic regimes. Because of varying rain characteristics with different climatic regimes, any developed IR method must be validated against appropriate *in situ* measurements taken over the region of interest before any application is made.

2.3.1   Cloud-Indexing Technique

Cloud-indexing technique rests on the observation that it is fairly easy to identify cloud types in satellite images and assign a rain rate to each cloud type. The rain at a particular location can then be written as

$$R \; = \; \sum r_i f_i, \tag{2.10}$$

where r_i is the rain rate assigned to cloud type i, and f_i is the fraction of time that the point is covered with cloud type i. The cloud-indexing technique was pioneered by Barrett (1970), he wanted to estimate precipitation over Australia and the 'Maritime Continent.' Barrett classified the cloud types into cumulonimbus, stratiform, cumuliform, stratocumuliform, and cirriform. He found that a cubic polynomial function of the satellite-estimated rain depth could account for 90% of the variance in rain-gauge-observed precipitation. Barrett (1973) attempted to forecast daily precipitation in another modification of the cloud-indexing technique.

Arkin (1979) proposed a simple rain estimation technique based on the relationship between radar-derived rainfall and fractional cloud coverage information collected over the area of 7° - 10° N, 22.5° - 24.75° W as a part of Global Atmospheric Tropical Experiment (GATE). It was shown that the maximum correlation between infrared window channel (10.5 – 11.5 µm) – hereafter referred to as $TB_{11,}$ and radar rainrate and uniform 3 mm/h rainrate was

produced if TB_{11} is less than 235 K. This technique is simple and useful for long-term and wide area rainrate estimation, but tends to underestimate rainrate associated with severe thunderstorms. The technique was not designed for pixel-scale instantaneous rainrate estimates but for acquiring rainfall climatologies over relatively large areas.

The most popular cloud-indexing technique was introduced by Arkin and Meisner (1987). They called their precipitation estimate the GOES Precipitation Index (GPI). They use a 235 K threshold and a constant rain rate of 3 mm/h, which are appropriate values for estimating tropical precipitation in areas approximately 2.5° X 2.5° of latitude. The precise equation is

$$GPI \quad = \quad 3\,f\,\Delta t, \tag{2.11}$$

where GPI is an estimate of the mean rain depth (mm) in the area, f is the fraction of area colder than the threshold, and Δt is the time (hours) for which f applies (if the images are collected each 3 h, then $\Delta t = 3$).

2.3.2   Bispectral Technique

Clouds that are bright in visible images are more likely to precipitate than dark cloud because brightness is related to optical depth and thus to cloud thickness. Clouds that are cold in infrared images are more likely to precipitate than warm clouds because cold clouds have higher tops than warm clouds. Bispectral methods attempt to combine these rules by saying that clouds, which have the best chance of raining, are both cold and bright.

Dittberner and Vonder Haar (1973) used a bispectral technique to estimate precipitation during the Indian Summer Monsoon. They developed a relationship of the form

$$P \;=\; c_1 E + c_2 A + P_o, \qquad\qquad (2.12)$$

where P is percent of normal seasonal precipitation, E is the seasonal mean infrared radiant exitance, A is the seasonal mean albedo, and the remaining parameters are regression coefficients.

Lovejoy and Austin (1979) compared SMS/GOES visible and infrared data with radar data in GATE and around Montreal. They used brightness and temperature observations together to determine whether it was raining. They constructed two 2D histograms: a raining histogram and non-raining histogram. The histogram axes were visible count (x-axis) and infrared count (y-axis). Twenty-five bins were used for each axis. The raining pixels are clustered near

the cold, bright portion of the histogram. The next step was to calculate precipitation probabilities for each bin as the ratio of the number of raining pixels to total pixels in each bin. These numbers are useful to map precipitation probabilities beyond the range of the radar. In the final step, Lovejoy and Austin determined a probability threshold to delineate raining pixels from non-raining pixels by minimizing a loss function (the fraction of incorrectly classified pixels). Lovejoy and Austin compared their bispectral technique to monospectral threshold techniques. The bispectral technique always performed better than either visible or infrared thresholds.

Tsonis and Isaac (1985) have modified the Lovejoy-Austin method using a clustering technique similar to those used for cloud detection. They delineate raining areas by classifying pixels in clusters. The raining cluster is determined from radar data. Tsonis and Isaac achieved a *probability of detection* (POD) of 66% and *false-alarm ratio* (FAR) of 37%. Eighty percent of the pixels were correctly classified. Tsonis and Isaac also found that their technique performs better for convective than for non-convective cases. In non-convective cases, the POD was higher, but the FAR was also higher.

2.3.3   Life-History Technique

The rain rate of a cloud, particularly a convective cloud, is a function of the stage in its life cycle. Life-history techniques take into account a cloud's life cycle. Geostationary satellite data are required for these techniques, and more than one image is necessary for the algorithms.

Stout *et al.* (1979) examined the relationship between radar-estimated rain and satellite-measured area of cloud for an isolated thunderstorm. The essential point is that the precipitation peaks while the cloud area is rapidly growing; precipitation is much reduced at the time of maximum cloud area. Stout *et al.* approximated this characteristic by adding a term to the rain-rate equation:

$$R \; = \; a_o A \; + \; a_1 \; (dA/dt) \tag{2.13}$$

where A is the cloud area, dA/dt is the time rate of change of the cloud area, a_o and a_1 empirically determined coefficients. Because a_1 is positive, this equation ensures that the rain rate will be larger in the growing stage than in the decaying stage of the cloud.

Griffith *et al.* (1980) began by comparing images (first visible, now infrared) with rain-gauge-calibrated Miami radar data. The scheme rests on an empirical attempt to estimate from satellite images what the associated radar echo for each cloud would be. To estimate the precipitation of a single cloud (colder than 253 K) it is first followed for its entire lifetime to determine its maximum areal extent (A_m). Clouds that merge or split are terminated, and the

resulting clouds are treated as new clouds. The empirical curves are used to determine the radar echo area from the satellite-estimated area of the cloud (A_c). The echo area (A_e) is estimated as a fraction of maximum cloud area depending on the ratio A_c / A_m and the sign of the time rate of change of A_c. A_m itself determines which curve to use. The rain rate is estimated using the curve and knowledge of the ratio of the echo area to the maximum echo area. The rain volume falling from the cloud is then the product of (1) the rain rate, (2) the echo area, (3) the time interval between successive satellite images, and (4) an empirical factor that starts at 1.00 and increases to a maximum of 3.24, essentially as the mean temperature of the cloud top decreases. Finally the total rain volume is apportioned within the cloud; one half of the rain falls uniformly below the coldest 10% of the cloud top, the remaining half falls below the next warmest 40% of the cloud top. No rain falls in the warmest half of the cloud. The Griffith – Woodley technique performed best for longer time periods and larger areas. This technique could not be considered useful for estimating how much rain falls in a single rain gauge, except, perhaps, for periods much longer than a day. Daily rainfall over a large area, however, is well represented by Griffith – Woodley, and an hourly precipitation is acceptable.

2.3.4   Cloud-Model Technique

To improve the precipitation estimation techniques based on visible and infrared satellite data, it is necessary to build the physics of the cloud into the retrieval process. Adler and Negri (1988), introduced the convective-stratiform technique (CST) by focusing on the precipitation in the presence of anvil clouds generated in the decaying stage of a convective system. The CST first identifies cirrus regions, and then defines convective cells using local minimum patterns in the IR temperature field. Rain estimation procedures are as follows:

a.   from cloud-top temperature distributions, local minima of cloud top temperature (T_{min}) less than 235 K are identified,

b.   by obtaining the average temperature (T_{ave}) of pixels surrounding an identified local minimum, a slope parameter ($S = T_{ave} - T_{min}$) is calculated,

c.   in order to discriminate minima introduced by thin cirrus clouds, an empirically pre-determined threshold value is applied – remaining minima are assumed to be precipitating areas with rain rates determined based on the result of a one- dimensional cloud model given by Adler and Mack (1984).

d.   anvil stratiform clouds are identified using a threshold temperature (T_s), obtained as a weighted mean over a region of 80 km x 80 km – pixels identified as stratiform clouds whose temperatures are lower than T_s, are assigned with constant rain rates of 2 mm/h.

Kurino (1997) developed an empirical algorithm estimating rainrate based on a statistical relationship between GMS three channels' brightness temperatures and radar estimated rainfall during a summer time period over a region around the islands of Japan. By relating radar-estimated rainfall to GMS-5 TB_{11}, split window channel difference (TB_{11} - TB_{12}) and ΔTB (i.e., $\Delta TB = TB_{11}$ - TB_{wv}), where TB_{12} and TB_{wv} are IR window channel (11.5 – 12.5 µm) and a water vapor channel (6.5 – 7.0 µm) brightness temperature respectively, a three-dimensional look-up table was developed from which rain probability and mean rainrate were determined for given GMS IR temperatures at each pixel. This method is described in greater detail in chapter 4.

2.3.5   Passive Microwave Technique

The advantage of the microwave portion of the spectrum is that microwave radiation penetrates clouds. Precipitation-size drops interact strongly with microwave radiation, which allow their detection by microwave radiometers. The disadvantage of microwave precipitation estimation techniques is that the radiometers have had poor spatial and temporal resolution. Three important properties of microwave estimation are:

- Ice essentially does not absorb microwave radiation; it only scatters.

- Liquid drops both absorb and scatter, but absorption dominates.

- Scattering and absorption both increase with frequency and with rain rate. However, scattering by ice increases much more rapidly with frequency than scattering by liquid.

Two general conclusions can be drawn. First, the microwave spectrum can be divided roughly into three parts. Below about 22 GHz, absorption is the primary mechanism affecting the transfer of microwave radiation. Above 60 GHz, scattering dominates absorption. Between 22 and 60 GHz, both scattering and absorption are important. Second, at different frequencies, microwave radiometers observe different part of rain structure. Below 22 GHz, any ice above the rain is nearly transparent; microwave radiometers respond directly only to the rain layer. Above 60 GHz, however, ice scattering is the dominant process; microwave radiometers sense only the ice and cannot see the rain below. Thus precipitation estimates made at higher frequencies are necessarily more indirect than those made at lower frequencies.

Precipitation estimates using microwave radiometry can be divided into two categories: absorption schemes and scattering schemes. Lovejoy and Austin (1980) pointed out two problems with the absorption approach to estimation of rain rate using passive microwave radiometry. Cloud water and rain water are difficult to separate, especially using a single wavelength. A combination of two problems exists: a beam-filling problem and non-linearity problem. Because of the inverse relationship between wavelength and antenna size required to

achieve a desired ground resolution, microwave radiometers have had large footprints, 500 km² at least. These areas are too large to be filled with a uniform rain rate. The radiometer averages the brightness temperature over the footprint, but because the brightness temperature is highly nonlinear in rain rate, the average brightness temperature will always underestimate the footprint mean rain rate.

The matter is further complicated by the difference radiative characteristics of sea and land surfaces. A sea surface has a relatively constant low emissivity (ε = 0.4) so that the radiation emitted from it is small and precipitation (ε = 0.8) will increase the amount of radiation detected by the sensor through emission. The high polarization of sea surface also contrasts very much with the low polarization of rain. Land surfaces have a high and variable emissivity (ε = 0.7 – 0.9) close to that of precipitation and low polarization. The emissivity is dependent upon the characteristics of the surface including vegetation cover and moisture content. Rainfall over land will increase the upwelling radiation stream but at the same time absorb radiation inducing errors in the identification of rain areas. Scattering is thus the key to microwave rainfall estimation techniques over land. Methods vary from relatively simple polarization techniques (Spencer, 1986; Spencer *et al.,* 1989) to more complex approaches based on cloud radiation models (Smith *et al*., 1992; Bennartz *et al*., 2002; Weng *et al*., 2003).

2.3.6   Hybrid Methods

Accurate and rapidly updated precipitation products for the atmospheric, oceanographic and hydrologic communities draw upon the use of multiple satellite sensors on geostationary and polar orbits. Sensors on geostationary metsats rapidly update imagery in the IR spectrum, which corresponds to emitted cloud top radiation for optically thick clouds. The SSM/I and AMSU from polar metsats provide a global coverage of precipitation.

Several infrared/microwave methods have been proposed trying to take advantage of the higher physical content of PMW measurements and the spatial and temporal coverage of geostationary metsats. Real-time products using SSM/I are available at the site http://www.nrlmry.navy.mil of the Naval Research Laboratory. An approach based on the synergetic use of GOES thermal IR data, radar instantaneous rainfall estimates and model output is the Auto-Estimator technique of NOAA NESDIS (Vicente *et al*., 1998).

Chapter 3　　Data Sets

The data sets for the research project were taken from various sources from the Malaysian Meteorological Services (MMS), the ASEAN Specialized Meteorological Center (ASMC) in Singapore and NOAA National Environment Satellite Data and Information Service (NESDIS) satellite active archives. Figure 3.1 shows the MMS observation network.

Figure 3.1　　Malaysian Meteorological Service observation network.

3.1 The Rain Gauge Data

The validation of satellite rainfall estimation algorithms is performed by using the rain gauge network established over Peninsular Malaysia. Figure 3.2 shows the location of the rain gauges currently maintained by MMS. They include the principal, climatological and rainfall stations. However, to ensure reliability and accuracy only the data set from twenty five (25) principal stations are used.
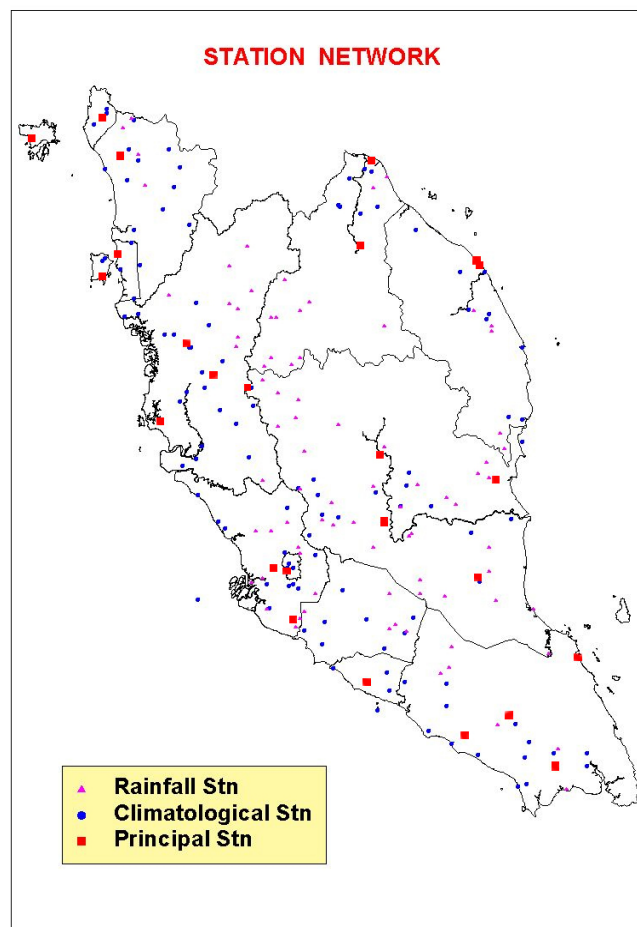
Figure 3.2   Distribution of the rain gauge network over
Peninsular Malaysia maintained by MMS.

The location of the Principal Stations where the rain gauge data was taken is listed in the table 3.1 below.

Table 3.1:   List of the principal station locations

	Station	Latitude	Longitude
01	Pulau Langkawi	99.73	6.33
02	Bayan Lepas	100.27	5.30
03	Butterworth	100.38	5.47
04	Alor Setar	100.40	6.20
05	Chuping	100.27	6.48
06	Kota Bharu	102.28	6.17
07	Kuala Krai	102.20	5.53
08	K.Terengganu Airport	103.10	5.38
09	K.Terengganu Climate	103.13	5.33
10	Sitiawan	100.70	4.22
11	Lubok Merbau	100.90	4.80
12	Ipoh	101.10	4.57
13	Cameron Highlands	101.37	4.47
14	Batu Embun	102.35	3.97
15	Subang	101.55	3.12
16	Petaling Jaya	101.65	3.10
17	Muadzam Shah	103.08	3.05
18	KLIA Sepang	101.70	2.73
19	Temerloh	102.38	3.47
20	Kuantan	103.22	3.78
21	Malacca	102.25	2.27
22	Batu Pahat	102.98	1.87
23	Kluang	103.32	2.02
24	Mersing	103.83	2.45
25	Senai	103.67	1.63

3.2   The Geostationary Metsat Data

Infrared measurements used in this study consist of two split-window channels (10.5 - 11.5 µm and 11.5 – 12.5 µm) and water vapor channel (6.5 – 7.0 µm); hereafter, the brightness temperature observed in these channels are referred to as TB_{11}, TB_{12}, and TB_{wv} respectively.

It is very unavoidable that during the study period, the winter monsoon 2001 to 2003, we have to rely on data from two different geostationary metsats, the Japanese Geostationary Meteorological Satellite-5 (GMS-5) and the NOAA Geostationary Operational Environmental Satellite-9 (GOES-9). The GMS-5 was launched in 1995 and had gone beyond its designed life span of five years and made its final observation at 00UTC on 22 May 2003.

Six days of hourly satellite observations were selected, consisting of three episodes of heavy rainfall events that occurred on 27 – 28 December 2001, 10 – 11 December 2002 and 8 – 9 December 2003. From 06UTC 22 May 2003, the Japan Meteorological Agency (JMA) started broadcasting GOES-9 GVAR (GOES Variable) data. GOES-9 was positioned at 155°E above the equator and used as backup while waiting for the launching of the Multi-Transport Satellite (MTSAT) in 2005. Figure 3.3 shows the location of study area from images from GMS-5 and GOES-9. Note the effect of the difference position of the two metsats, particularly in the area of Peninsular Malaysia which is much closer to the edge of the GOES-9 coverage area than that of GMS-5.
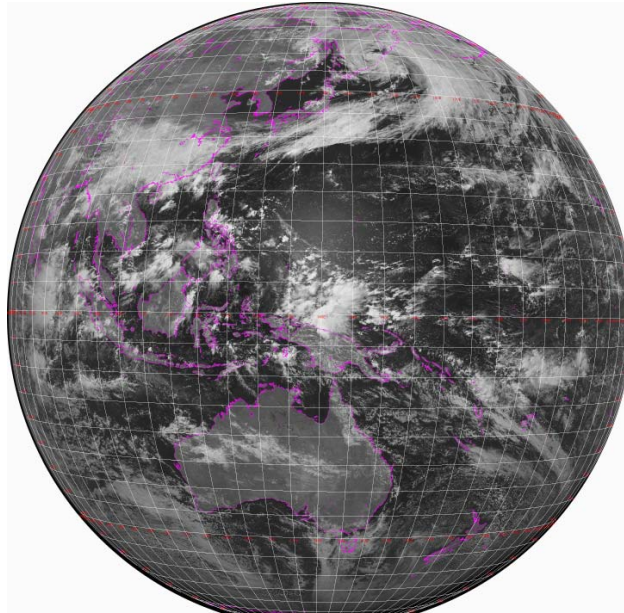
(a) GMS-5 IR imagery
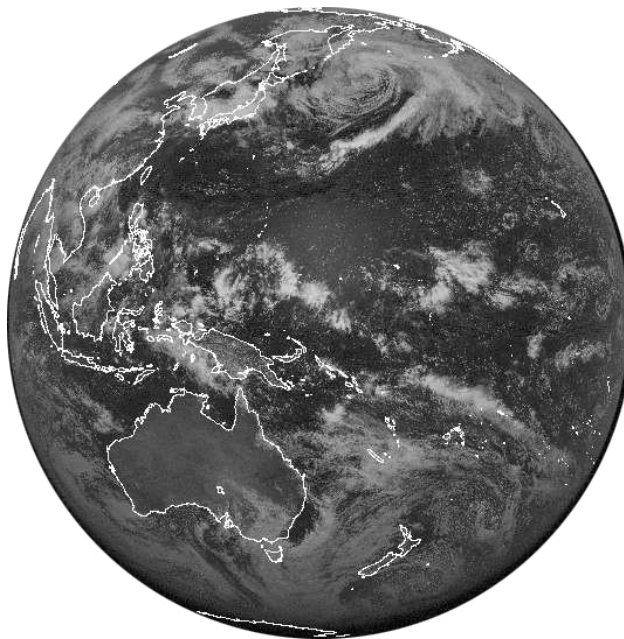
(b) GOES-9 IR Imagery

Figure 3.3   Effect of position of GMS-5 (140ºE) and GOES-9 (155ºE)
on satellite imagery.

3.3 The Polar-Orbiting Metsat Data

The Polar-Orbiting Operational and Environmental Satellites (POES) satellite system offers the advantage of daily global coverage, by making nearly polar orbits roughly 14.1 times daily.

The Passive Microwave (PMW) instruments onboard of NOAA KLM spacecrafts are the Advanced Microwave Sounding Units (AMSU) system. The system consists of two separate modules: the AMSU-A and AMSU-B. The AMSU-A is a 15-channel microwave radiometer that is used for measuring global atmospheric temperature profiles and provides information on atmospheric water in all of its forms (with exception of small ice particles, which are transparent at microwave frequencies). The AMSU-B is a 5-channel microwave radiometer. The purpose of the instrument is to receive and measure radiation from a number of different layers of atmosphere in order to obtain global data on humidity profiles. It works in conjunction with the AMSU-A instruments to provide a 20-channel microwave radiometer. The center frequencies and bandwidths of the AMSU channels are listed in Table 3.2 (Staelin and Chen, 2000). The microwave characteristics of the atmosphere are shown are in Fig. 3.4. AMSU-B covers channels 16 through 20. The highest frequency channels, (18, 19 and 20), span the strongly opaque water vapor absorption line at 183 GHz and provide data on the atmosphere's humidity level. Channels 16 and 17, at 89 GHz and 150 GHz, respectively, enable deeper penetration through the atmosphere to the Earth's surface (Goodrum *et al*., 2001).

Table 3.2   AMSU channel characteristics

AMSU-A Channels

Channel	Center Frequency (MHz)	Bandwidth (MHz)	Polarization	Nadir Spatial Resolution (km)
1	$23{,}800 \pm 72.5$	2 x 125	V	50
2	$31{,}400 \pm 50$	2 x 80	V	50
3	$50{,}300 \pm 50$	2 x 80	V	50
4	$52{,}800 \pm 105$	2 x 190	V	50
5	$53{,}596 \pm 115$	2 x 168	H	50
6	$54{,}400 \pm 105$	2 x 190	H	50
7	$54{,}940 \pm 105$	2 x 190	V	50
8	$55{,}500 \pm 87.5$	2 x 155	H	50
9	$f_0 = 57{,}290.344 \pm 87.5$	2 x 155	H	50
10	$f_0 \pm 217$	2 x 77	H	50
11	$f_0 \pm 322.2 \pm 48$	4 x 35	H	50
12	$f_0 \pm 322.2 \pm 22$	4 x 15	H	50
13	$f_0 \pm 322.2 \pm 10$	4 x 8	H	50
14	$f_0 \pm 322.2 \pm 4.5$	4 x 3	H	50
15	$f_0 \pm 8{,}900 \pm 900$	2 x 1000	V	50

AMSU-B Channels

Channel	Center Frequency (MHz)	Bandwidth (MHz)	Polarization	Nadir Spatial Resolution (km)
1	89 ± 1	2 x 1	V	16
2	150 ± 0.9	2 x 1	V	16
3	183.31 ± 1	2 x 0.5	V	16
4	183.31 ± 3	2 x 1	V	16
5	183.31 ± 7	2 x 2	V	16
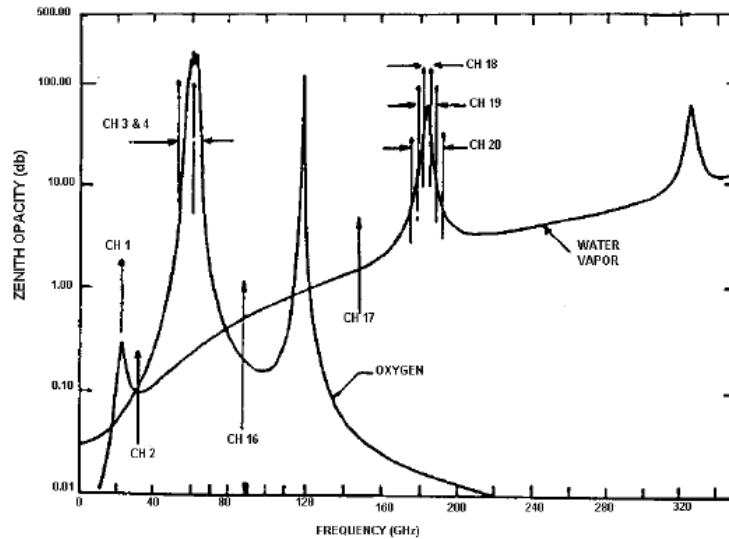
Figure 3.4   Microwave characteristics of the atmosphere
              (from http://www2.ncdc.noaa.gov/docs/klm).

For the development of statistical algorithms using the probability matching method and calibration purposes we used the 15-km resolution 89-191 GHz module of AMSU derived rainrate onboard NOAA 15, 16 and 17 satellites to match with the Look-Up Table (LUT) technique (Kurino, 1997). The AMSU rainrate algorithm used in this study is the NESDIS algorithm based on scattering processes (Chen and Staelin, 2003). Table 3.3 listed the dates and times of the NOAA satellite overpasses used in this study.

Table 3.3   List of dates and times of the NOAA satellites
overpasses used in the study.

Date	Time (Z)	Satellite
27/12/2001	00:26	NOAA-15
27/12/2001	06:38	NOAA-16
27/12/2001	19:22	NOAA-16
10/12/2002	00:39	NOAA-15
10/12/2002	03:48	NOAA-17
10/12/2002	06:47	NOAA-16
10/12/2002	11:40	NOAA-15
10/12/2002	14:49	NOAA-17
10/12/2002	19:29	NOAA-16
11/12/2002	00:15	NOAA-15
11/12/2002	06:35	NOAA-16
08/12/2003	07:19	NOAA-16
09/12/2003	03:39	NOAA-17

Since the spatial resolution of each GMS IR pixel is about 5 km at the sub-satellite point, all pixels located within a 0.05° x 0.05° box are averaged in order to relate IR brightness temperatures to AMSU estimated rainrate. This is done by comparing each AMSU overpass with the nearest geostationary metsat image in time and by collecting data for three winter monsoons of 2001, 2002 and 2003 over the analysis domain bounded by 0° - 8° N and 100° – 105° E. Thus, a set of matched pairs of AMSU derived rainrate and IR brightness temperatures is generated, in which IR brightness temperatures now retain the same temporal and spatial resolution as the AMSU.

Chapter 4   Methodology

4.1   Overview

This study used a look-up table (LUT) technique to estimate rainrate (Kurino, 1997) based on geostationary metsats hourly observations. A comparison was done by matching the pixels ($0.05°$ by $0.05°$) in the satellite estimate that corresponds to the rain gauge value recorded at the 25 principal stations distributed over Peninsular Malaysia. A cumulative hourly rainfall for heavy rain cases (a total of more than 40 mm a day) recorded at a particular station was used for this comparison.

When the polar metsats passed over the area of study, the microwave rainrate using NESDIS AMSU algorithm was used to calibrate the LUT rainrate estimate. A scatter plot was then produced from the rainrate values of both algorithms, and the second, third and fourth degree polynomial curves fitted to obtain a relationship between the two algorithms. The LUT data are then corrected using one of the polynomial curves. A cumulative hourly rainrate of the microwave corrected LUT (MWL) is then compared with the recorded rain gauge values (RGV).

Further comparison was also done using both hourly and daily values of MWL, LUT and RGV by employing both the probability and statistical analysis. The probability matching method was employed to compare the performance of RGV, LUT and MWL (Oh *et al.*, 2002).

4.2　　　The Look-Up Table Technique

Kurino (1997) developed an empirical algorithm estimating rainrate based on a statistical relationship between GMS three-channel brightness temperatures and radar estimated rainfall during a summer time period over a region around the Okinawa islands of southern Japan. By relating radar-estimated rainfall to GMS-5 TB_{11}, split window channel difference ($TB_{11} - TB_{12}$) and ΔTB, the difference between TB_{11} and TB_{wv} (i.e., $\Delta TB = TB_{11} - TB_{wv}$), a three dimensional look-up table was developed from which probability of rain and mean rainrate were determined for the given GMS IR temperature at each pixel.

The IR split window channels (11 μm, 12 μm) is used in detection of Cirrus (Ci) cloud. If $TB_{11} - TB_{12}$ is more than or equal to 3 K, it indicates the presence of thin cirrus, thus no rainfall is expected from the cloud. ΔTB is useful for extracting deep convective cloud with heavy rainfall (Inoue, 1987). Ackerman (1996) theoretically showed that for the tropics and mid-latitudes, typically thick clouds produce rain when ΔTB value is greater than -5 K.

Results from Kurino (1997) are shown in Fig. 4.1 and Fig. 4.2. Figure 4.1 is a scatter diagram of TB_{11} and $TB_{11} - TB_{12}$ for raining pixels from radar observations. Figure 4.2 is a scatter diagram of TB_{11} and ΔTB for heavy rain pixels (20.0 mm/h) from radar observation.
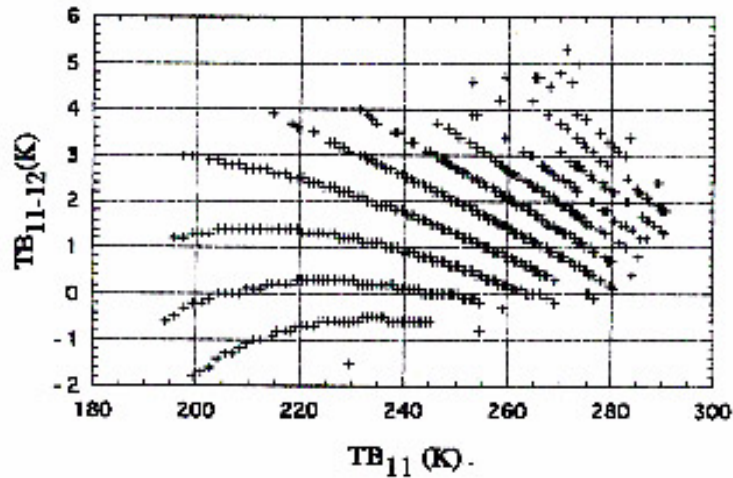
Figure 4.1   The scatter diagram of raining pixels in case of Typhoon Ryan.
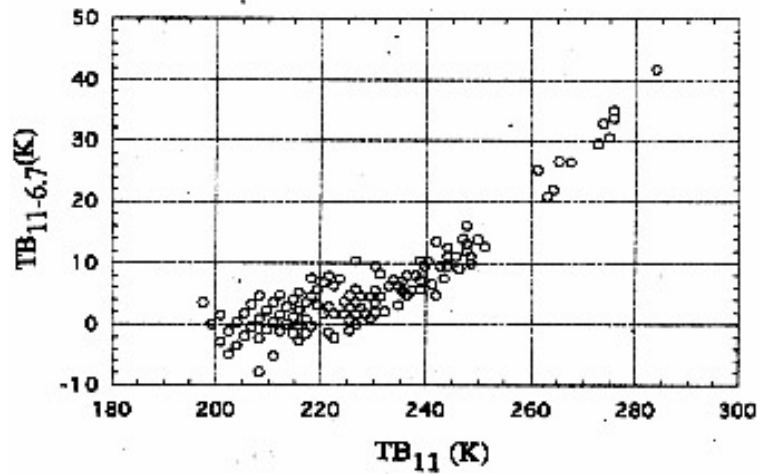
Figure 4.2   The scatter diagram of heavy raining pixels
(over 20.0 mm/h) in case of Typhoon Ryan.

45

For this study a total of 144 images using LUT algorithm were produced for the entire study period with each image having a total of 16 000 pixels of 0.05° by 0.05° covering the area of study. Figure 4.3 shows a sample of the rainfall estimate using LUT method when Tropical Storm Vamei made landfall over southeastern tip of peninsula.
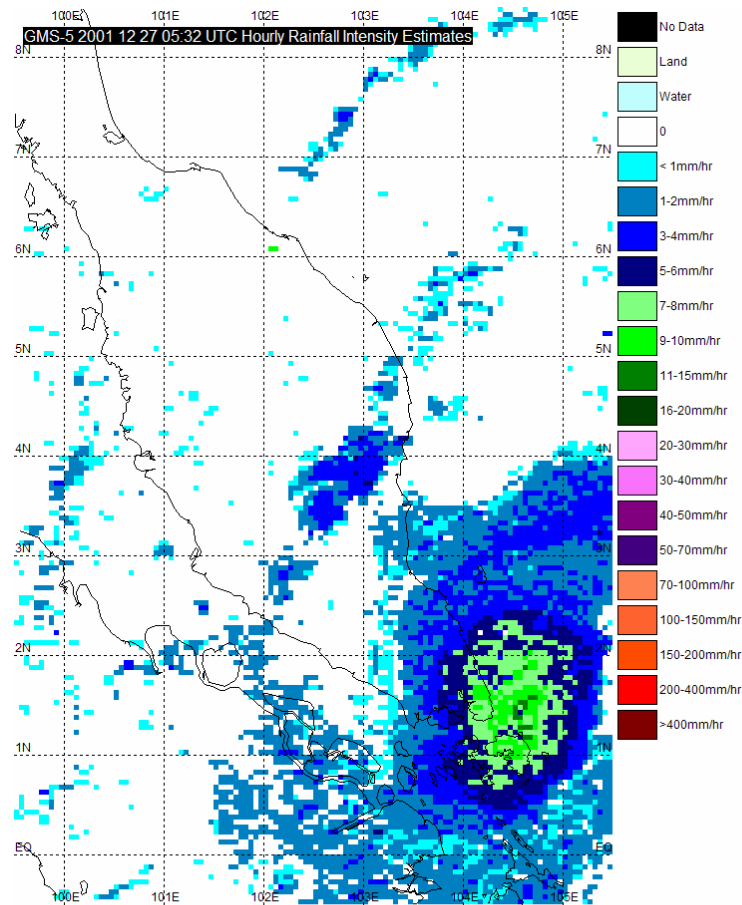
Figure 4.3   Tropical Storm Vamei using LUT rainrate estimate

4.3   The NESDIS AMSU Rainrate Algorithm

The NESDIS AMSU rain rate algorithm (RR) is retrieved by converting Ice Water Path (IWP) into surface rainfall rate using the Goddard precipitation profiling algorithm data sets that contain the profiles of various hydrometeors generated from cloud model (Kummerow *et al*., 2001). The relationship takes the form

$$RR \quad = \quad r_0 + r_1 IWP + r_2 IWP^2 \qquad\qquad (4.1)$$

where r_0, r_1 and r_2 are the correlation coefficients, *RR* is in mm h^{-1} and *IWP* is in kg m^{-2}. IWP is directly proportional to the ice cloud scattering parameter Ω. By assuming that the ice particle size distribution follows a gamma distribution and Ω is calculated using Mie theory, the IWP can be expressed in terms of the effective particle diameter D_e and the ice particle bulk volume density ρ (Zhao and Weng, 2002 and Weng *et al*., 2003)

$$IWP \quad = \quad \mu\, D_e\, \rho\, (\Omega / \Omega_N) \qquad\qquad (4.2)$$

where μ is the cosine of the satellite look zenith angle and Ω_N is the normalized scattering parameter that is only dependent on particle effective size and complex index of refraction. Finally, assuming a modified Gamma size distribution and a constant ice particle bulk volume density, the regression relationships of $D_e - r$ and $\Omega_N - r$ are obtained as follows

$$D_e \quad = \quad a_0 + a_1 r + a_2 r^2 + a_3 r^3 \qquad\qquad (4.3)$$

$$\Omega_N \quad = \quad exp\, (b_0 + b_1 ln\,(D_e) + b_2 ln\,(D_e)^2) \qquad\qquad (4.4)$$

where $r = \Omega_{89} / \Omega_{150}$ is the scattering parameter ratio between Ω at 89 GHz and 150 GHz; a_i (i = 0, 1, 2, 3) and b_i (i = 0, 1, 2) are coefficients that are dependent on ice particle bulk density and size distribution. Given ρ and D_e then subsequently IWP can be uniquely determined. Recent improvements to this algorithm include a two-stream correction of the TB_{89} and TB_{150} as a function of μ. Two sets of values for the a_i and b_i coefficients that have been employed based upon the value of D_e are presented in Table 4.1 (Ferraro *et al*., 2005).

Table 4.1.　The coefficients used in the D_e and *IWP* algorithms.

		a_0	a_1	a_2	a_3
D_e		-0.300323	4.30881	-3.98255	2.78323
			b_0	b_1	b_2
IWP	$D_e < 1.2$ mm	-0.294459	1.38838	-0.753624	
	$D_e \geq 1.2$ mm	-1.19301	2.08831	-0.857469	

It was found that three sounding channels at 183±1, ±3, ±7 GHz are sensitive to the water vapor at different atmospheric levels. An indicator of the convective strength index (CI) of cloud systems is defined and calculated based on the information inferred from the AMSU 183-GHz measurements. Specifically, CI is defined as a series of brightness temperature differences

$$\Delta_1 \quad = \quad TB_{183\pm1} \quad - \quad TB_{183\pm7}$$

$$\Delta_2 \quad = \quad TB_{183\pm3} \quad - \quad TB_{183\pm7}$$

$$\Delta_3 \quad = \quad TB_{183\pm1} \quad - \quad TB_{183\pm3} \tag{4.5}$$

when conditions below are satisfied,

$$CI = \quad 1 \text{ when } \Delta_2 > 0, \ \Delta_2 > \Delta_1, \text{ and } \Delta_2 > \Delta$$

$$CI = \quad 2 \text{ when } \Delta_1 > 0, \ \Delta_2 > 0, \ \Delta_3 > 0, \ \Delta_1 > \Delta_2, \ \Delta_1 > \Delta_3, \text{ and } \Delta_2 > \Delta_3$$

$$CI = \quad 3 \text{ when } \Delta_1 > 0, \ \Delta_2 > 0, \ \Delta_3 > 0, \ \Delta_1 > \Delta_2, \ \Delta_1 > \Delta_3, \text{ and } \Delta_3 > \Delta_2 \tag{4.6}$$

where CI = 1 (weak convection or stratiform rain), CI = 2 (moderate convection), and CI = 3 (strong convection).

Effectively they are producing an objective storm-type classification (or rain typing) before applying a suitable RR algorithm. Presently, two sets of coefficients are used,

For CI = 1 or 2, $\quad RR \quad = \quad 0.322 + 16.504 IWP - 3.342 IWP^2$ (4.7)

For CI = 3, $\quad RR \quad = \quad 0.089 + 20.819 IWP - 2.912 IWP^2$ (4.8)

The maximum allowed rain rate for this algorithm is 30 mm/h; this seems to be the limitation when the actual rainrate can be much heavier. It is found that the AMSU-derived cloud ice water path is highly correlated with the surface rainfall rates and it is now directly used to monitor surface precipitation throughout the world (Zhao and Weng, 2002).

4.4   Adjusting the LUT Algorithm

Having acquired coincident IR and PMW data, the following procedure was used to adjust the LUT values using PMW rainrate. The hourly LUT rain rate pixels were matched with NESDIS AMSU rain rates when the polar-orbiting metsats overpass the raining region in the study area. Thus, a set of 150 matched pairs of AMSU-derived rain rates and IR brightness temperatures is generated and a scatter plot is produced with second, third and fourth orders polynomial best fit curves as shown in Fig. 4.4.

The data were aligned in the vertical orientation due to the discrete values used in the estimation of rain rate using LUT technique. Table 4.2 gives the correlation coefficients and residuals for each order of polynomial. As expected the residuals were quite large due to the data orientation. For this study we chose the quadratic polynomial curve for adjusting the LUT rainrate with the NESDIS AMSU rainrate since there are only small variances between the curves and the quadratic curve does not reduce above rainrate of 15 mm/h.
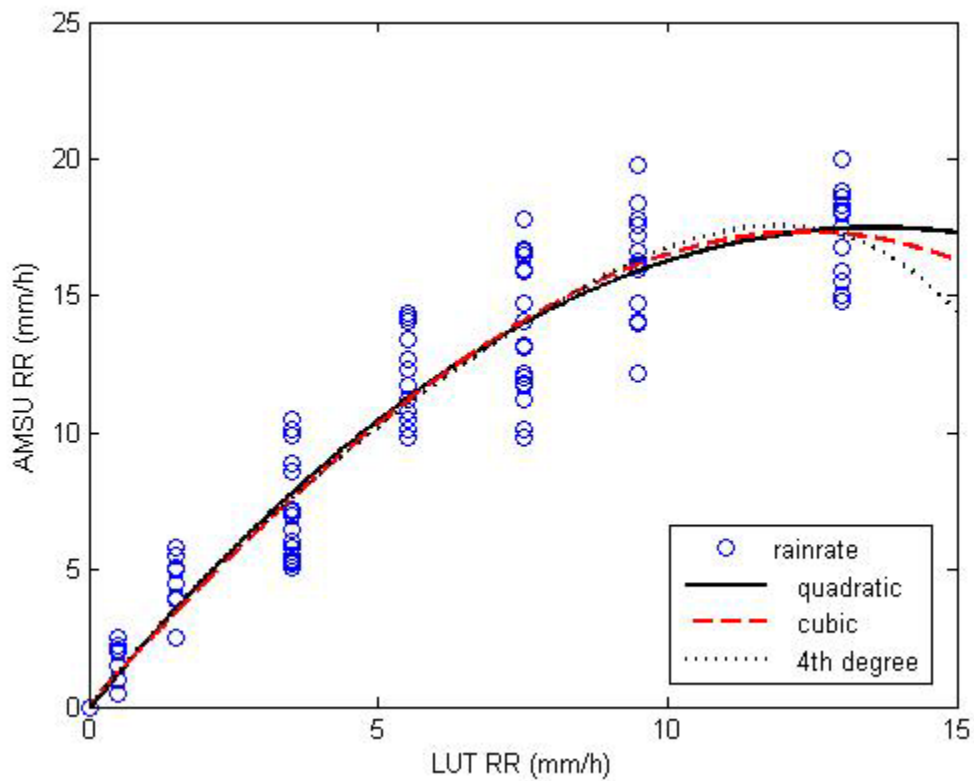
Figure 4.4   Relationships between AMSU and LUT rainrate estimates
using 2nd-, 3rd- and 4th-degree polynomial curves.

Table 4.2 shows that the residual for the 4th degree polynomial is 18.36 while the quadratic curve is 18.49 which is only a difference of 0.13. So the equation used to correct the LUT values based on the comparison with PMW rainrate is:

$$MWL = -0.095*LUT^2 + 2.582*LUT - 0.044 \hspace{2cm} (4.9)$$

This adjustment is then applied across the entire field and at times with the IR imagery not coincident with PMW. The corrected LUT values (MWL) were then compared with RGV using some of the statistical analysis methods as described in section 4.5.

Table 4.2   Correlation coefficients for 2nd-, 3rd- and 4th-degree polynomial curves in Fig. 4.3

Coefficients	p_1	p_2	p_3	p_4	p_5	Residual
Quadratic	-0.095	2.582	-0.044			18.49
Cubic	-0.003	-0.033	2.287	0.150		18.40
4th Degree	-0.001	0.017	-0.191	2.673	0.018	18.36

4.5   The Statistical and Probability Analysis

To objectively evaluate the quality of the LUT rainrate algorithm and the MWL rainrate algorithm as compared to RGV we used some statistical and probability verification techniques as suggested by Wilks (1995).

4.5.1   Basic Statistical Treatments

For inter-comparison between various rain retrievals for all the three cases, the mean rainrate, standard deviation of RGV values, LUT and MWL estimates were calculated. The root mean square errors (RMSE), biases and correlation coefficients (Corr) of LUT and MWL as compared to RGV were also obtained.

4.5.2   Scatter Plots and Regression Analysis

The scatter plot is probably the simplest verification tool. Using the 45 degree line or linear line of y = mx, where m = 1 to represent a better estimate. Scatter diagrams with least squares regression lines were plotted for the LUT and MWL data using RGV as the independent variable. If the estimates were perfect, this line would coincide with the 45 degree line. Correspondence between the regression line and the 45 degree line is simply the measure of reliability. A comparison of the slope of the regression line and the 45 degree line

gives a visual representation of the relative quality of the estimates. As the quality decreases, the regression line tends more toward the horizontal. A horizontal line means no skill.

4.5.3   Probability Matching Method

The probability matching method employed here is the slight modification from Oh *et al*., 2002; this technique has been used in the rainfall estimation using radar reflectivity. Using the hourly rainrate at each of the 25 stations, we calculated the probability of rain (PoR), mean rainrate (mRR), total rainrate (tRR) and, finally, derived the rainrate (RR) in each measurement technique; the RGV, LUT and MWL. For each of our case studies, we have a total of 1200 observations made up of 2 days hourly observations at 25 sites. These values were used to evaluate the performance of the LUT and MWL as compared to the RGV. The following definitions were adopted,

$$PoR \quad = \quad Nr / (Nr + Nnr) \hspace{3cm} (4.10)$$

where Nr and Nnr are rain and no rain frequencies respectively,

$$mRR \quad = \quad tRR / Nr \hspace{3.5cm} (4.11)$$

then finally, the *RR* was derived by,

$$RR \quad = \quad mRR * PoR \hspace{3.5cm} (4.12)$$

Chapter 5   Results and Discussion

In this chapter three case studies are presented. Case 1 is a tropical storm case, while the other two are monsoonal rain cases. Cases 1 and 2 used GMS data, while case 3 used GOES data. For each case a description of the event is followed by presentation and discussion of the rainfall estimation results.

5.1   27-28 December 2001 Case

5.1.1   Event Overview

Tropical Storm Vamei, which occurred over the South China Sea on 26th December 2001, was the most unusual and perhaps the most unique storm of the season for two reasons. Firstly, it was designated as having typhoon strength at the exceptionally low latitude of 1.5°N, and secondly, it was the first tropical storm to have crossed Peninsular Malaysia in recorded history. The previous recorded lowest latitude for a typhoon was 3.3°N for Typhoon Sarah in 1956.

Did Vamei actually attained typhoon or for that matter tropical storm intensity is a topic of debate. The cloud development around the system as inferred from infrared satellite imageries and Doppler radar imageries had a spiral band structure similar to ones associated with active tropical storms or typhoons. The Joint Typhoon Warning Center (JTWC) classified the system as a typhoon based on US naval ship observations of the wind speed. However these reports could not be independently verified. Surface wind speed and barometric readings from principal meteorological stations nearest to the path of the storm do not fulfill the criteria for the storm to be of tropical storm intensity (Moten, 2003).

On 25th December 2001 a monsoon disturbance developed over the South China Sea. The system remained quasi-stationary but slowly intensified with a well-organized cloud system forming around the center as observed from satellite images. At 0000Z on 27 December, JTWC classified the system as Typhoon Vamei based on US naval ship observations, indicating sustained winds within the small eye wall of 75 knots with gusts of 105 knots. This storm developed from a monsoon depression located around 1.5°N, 106.6°E on 26/1200Z. It attained typhoon intensity with a maximum intensity of 75 knots on 27/0000Z at around 1.5°N, 105.0°E and by 0600Z it made landfall on the southeast coast of Malaysia Peninsula. Thereafter, it weakened into a tropical storm, but continued its movement in a westerly direction. On 28/0000Z, it dissipated into a tropical depression over the Straits of Malacca.

The 12-h precipitable water analyses and LUT rainfall estimate on 27 – 28 December 2001 are shown in Fig. 5.1 (http://www.cdc.noaa.gov/cdc/ reanalysis/) and Fig. 5.2 respectively. The analyses showed that the storm affected the southeastern region on 27 December and moved to the northwestern states the following day.
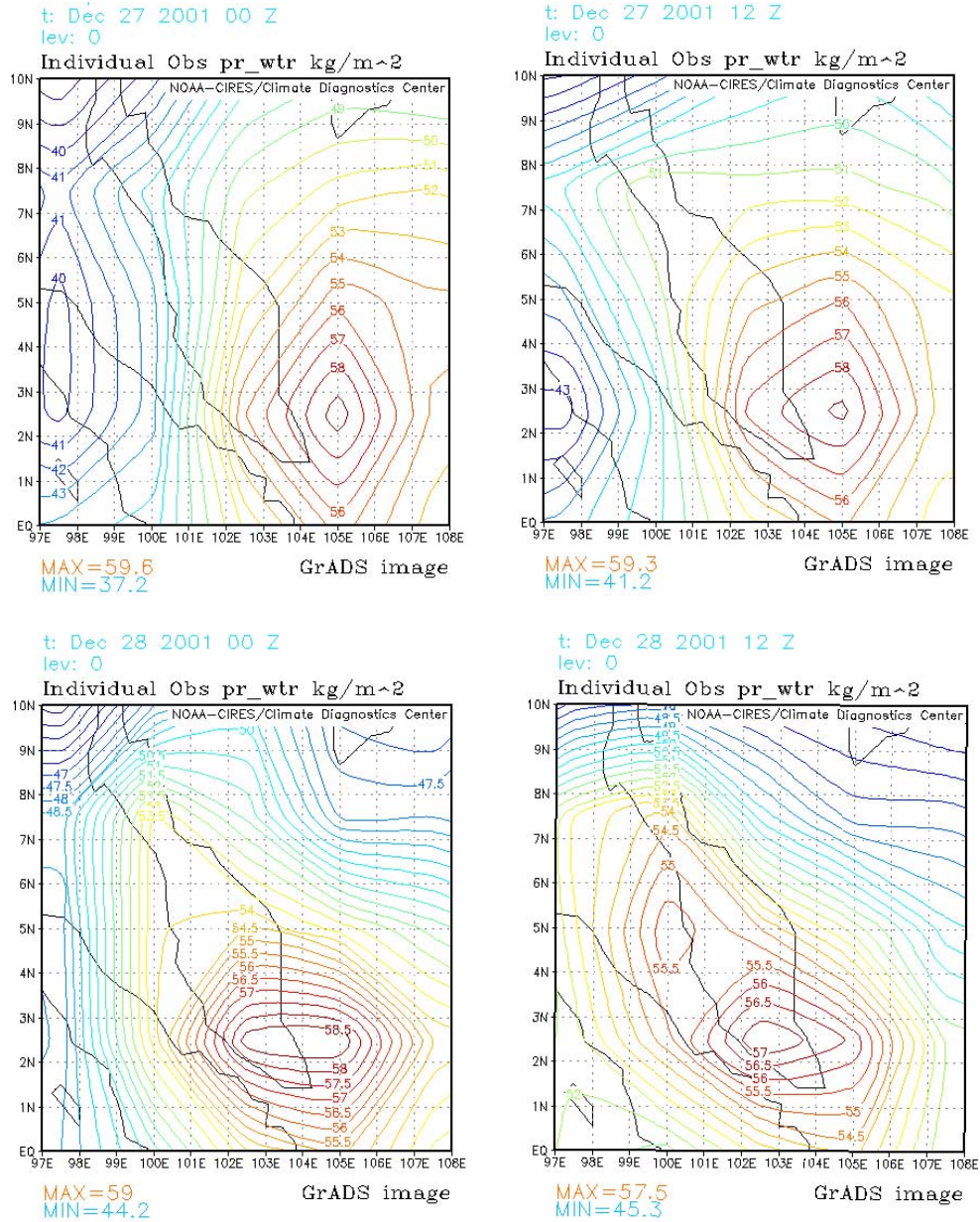

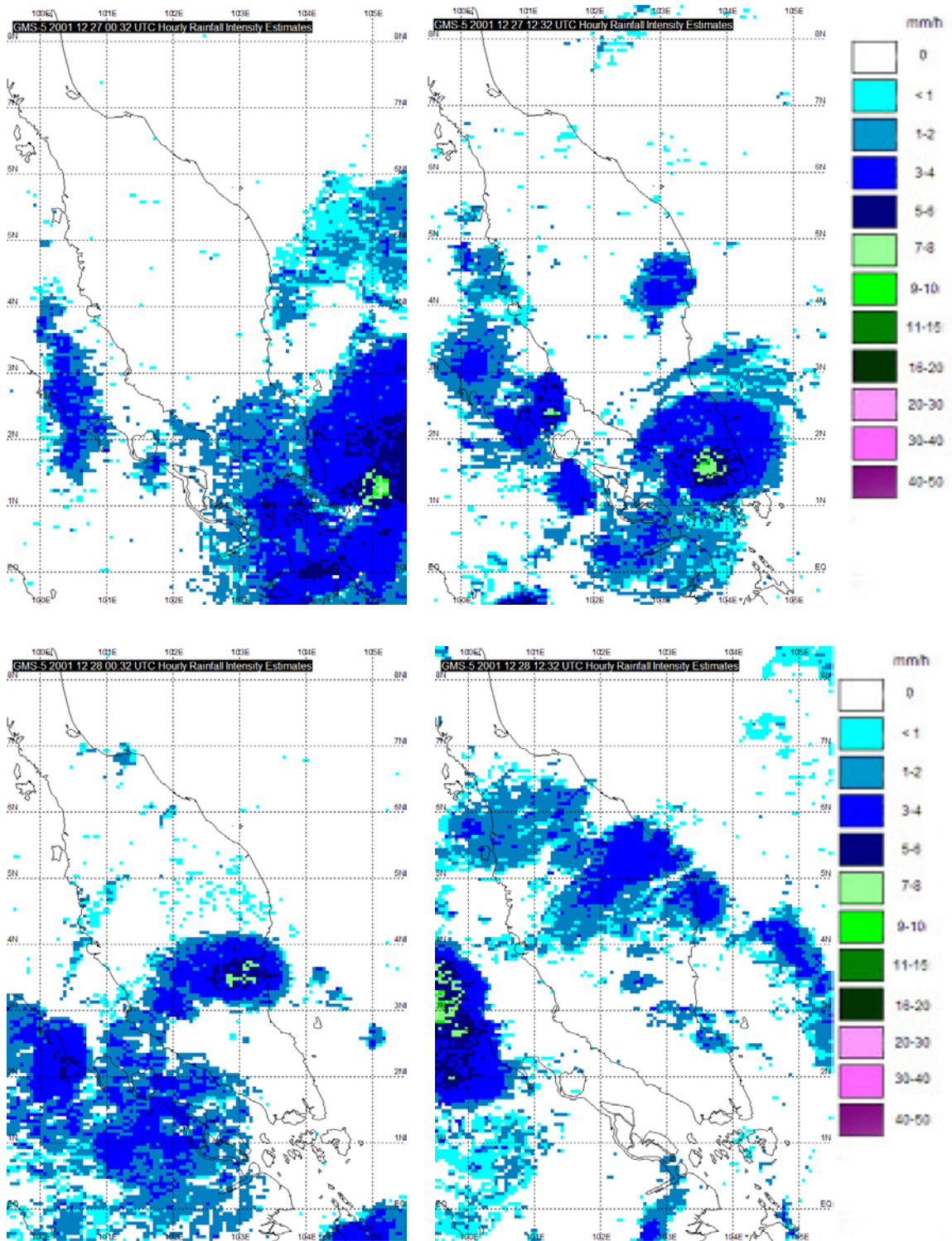Figure 5.1   The 12-h analyses of precipitable water
on 27-28 December 2001.

Figure 5.2   The 12-h LUT rainrate estimate on 27-28 December 2001.

5.1.2   Results and Discussion

The hourly cumulative rain comparison between the RGV and LUT, for eight rain gauge sites on 27 Dec 2001 is shown in Fig. 5.3. The LUT estimates seem to do well when the total cumulative rainfall is 20 mm or less. When total cumulative rainfall increases LUT estimates appear to underestimate the values for all of the cases. The difference in values gets larger when there are outbursts of heavy rainfall in a short period of time. These are clearly indicated in all the cases above. After adjusting the LUT estimate with the NESDIS AMSU rainrate as shown in Fig. 5.4, we found that the MWL estimate gave a better result except for the cases of Muadzam Shah and Batu Pahat on 27 December 2001 where MWL overestimates the rainfall amount. For both of these cases the total accumulative rainfall amount from RGV is relatively small, 48.1 mm and 65.7 mm respectively. However, if we examine the wind speed observations from this area, it is likely that the gauges are under-recording the rainfall due to the wind drift.

For the case of extremely heavy rainfall in a few hours as of Senai on 27 December 2001 even the MWL is not able to give a good estimate, this is mainly due to the nature of the satellite observation itself. It is mainly due to two factors, the temporal and spatial resolution of satellite's observations. The temporal resolution of hourly observations is not sufficient to observe heavy rainfall outbursts which last less than an hour especially if the burst occurs between observations. In most occasions over the tropical regions heavy rain bursts lasted only for 20 to 30 minutes. The spatial resolution of 5 km for GMS-IR

and 15 km for NOAA-PMW estimates is another limitation. The tropical rainfalls are more localized in nature, occurring over areas smaller that satellite resolution. The other important factor is the time lag between the satellite and rain gauge observations that can contributes to the disparity in the estimated values. The wind drifts especially in the case of the storm will also significantly contribute to the under-recording of the rainfall by the gauges.
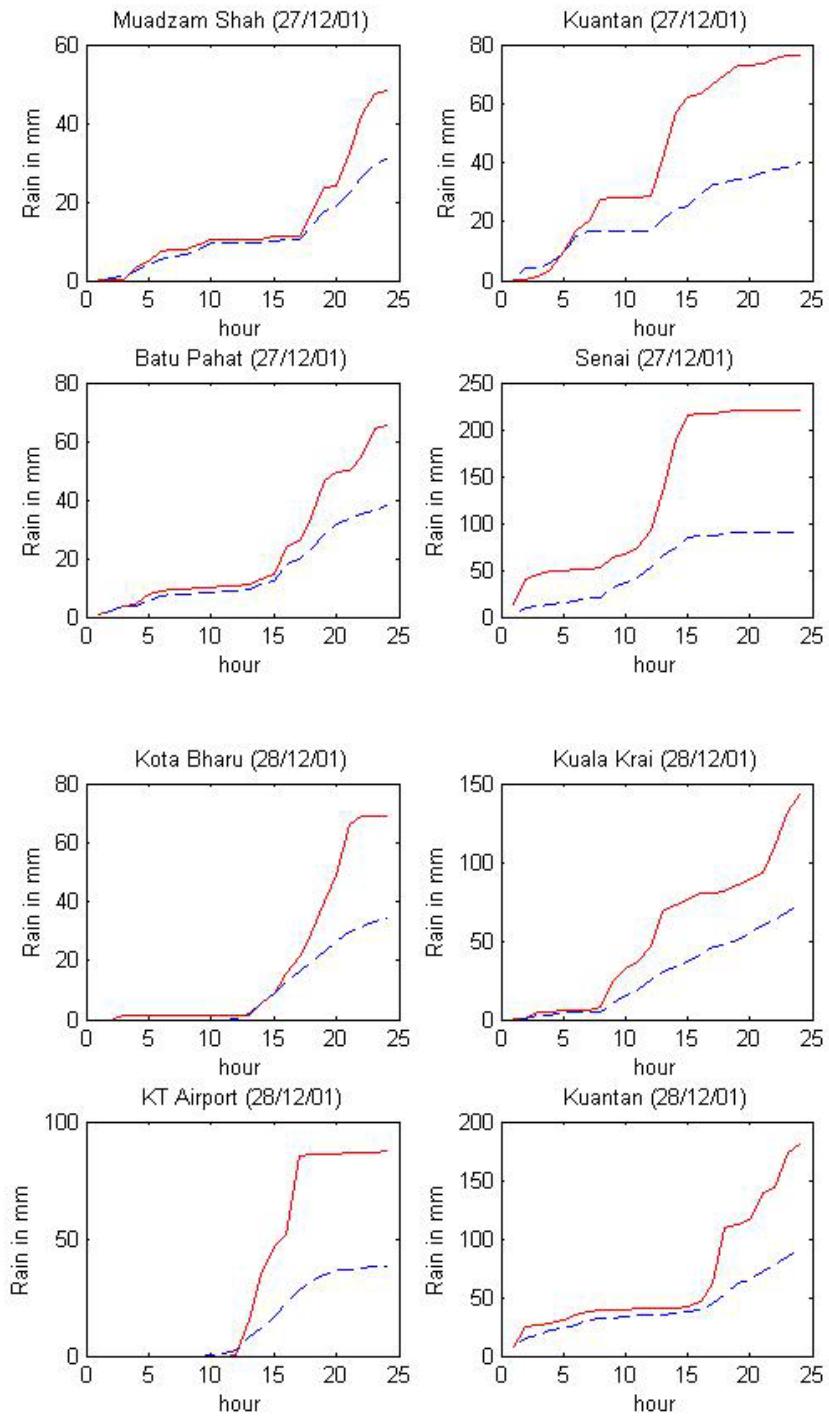
Figure 5.3   Cumulative rainfall for LUT (---) and RGV (—).
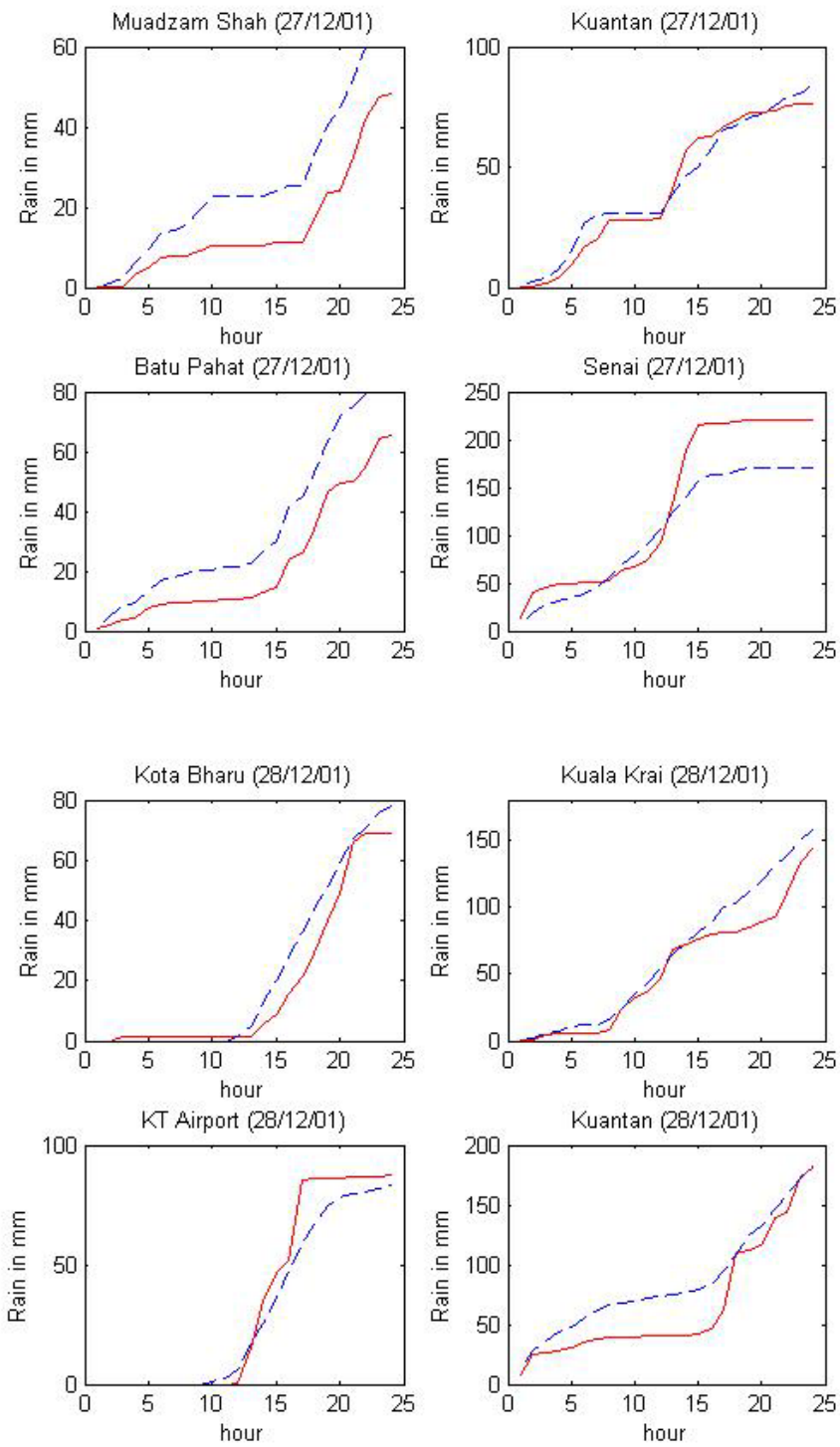
Figure 5.4   Cumulative rainfall for MWL (---) and RGV (—).

By examining the cumulative rainfall we find that in the early stages, the LUT estimate performed better than the MWL for the storm case, while the second half of the period when the accumulated rainfall amount started to increase to above 600 mm, the MWL estimate began to perform better than LUT as shown cumulative curves in Fig. 5.5 and the percentage errors (PE) in Table 5.1.
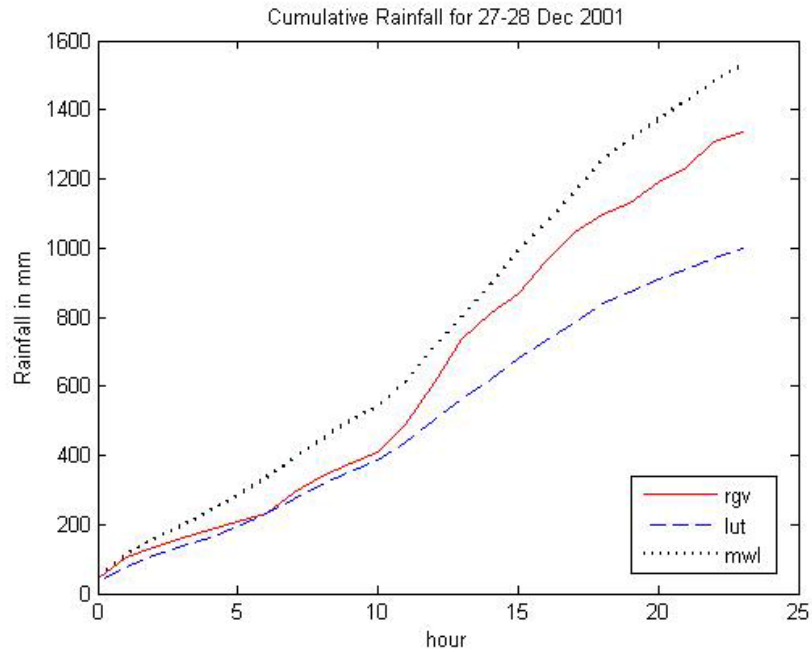
Figure 5.5   Cumulative rainfall for LUT (---), RGV (—)
and MWL (**…**) for 27-28 December 2001.

Table 5.1   Percentage error of LUT and MWL cumulative rainfall
            compared to RGV as in Fig. 5.5.

Time(Z)	00	01	02	03	04	05	06	07	08	09	10	11
LUT	17.7	26.3	17.7	16.7	12.5	7.7	1.4	5.9	7.1	6.4	6.5	10.4
MWL	12.7	5.1	17.6	19.7	27.5	36.0	42.9	33.7	30.7	31.8	32.3	25.9

Time(Z)	12	13	14	15	16	17	18	19	20	21	22	23
LUT	17.2	23.6	23.6	21.5	23.7	24.9	23.4	22.5	23.6	23.9	25.6	25.1
MWL	16.8	8.6	9.8	14.0	12.0	11.1	14.4	16.4	15.5	15.6	13.4	14.5

For case 1, the average percentage error for LUT is 17.3% and that of
MWL is 19.9%, both the averages are relative small, which indicates that both
MWL and LUT estimates performed quite well with LUT was marginally better.

5.2   10-11 December 2002 Case

5.2.1   Event Overview

On 10 December 2002, a monsoon surge started affecting the northern and central regions of the east coast of Peninsular Malaysia. Heavy rainfalls were recorded over Kota Bharu, KT Airport, KT Climate and Kuantan which read 149.2, 182.2, 169.6 and 89.2 mm, respectively. It continued the following day, migrating slightly southward with slightly lower intensity. The rainfalls recorded over KT Airport, KT Climate and Kuantan for December 11 were 96.6, 113.6 and 67.6 mm, respectively.

The 12-h precipitable water analyses on 10 – 11 December 2002 is shown in Fig. 5.6 (http://www.cdc.noaa.gov/cdc/reanalysis/) and Fig. 5.7 shows the 12-h LUT rainfall estimate. The analyses showed the affected regions.
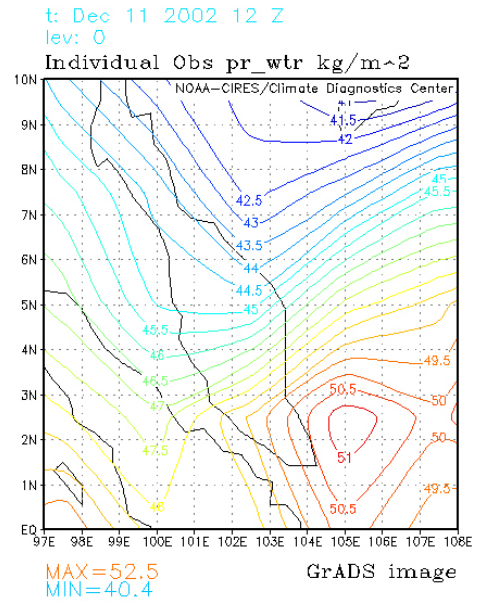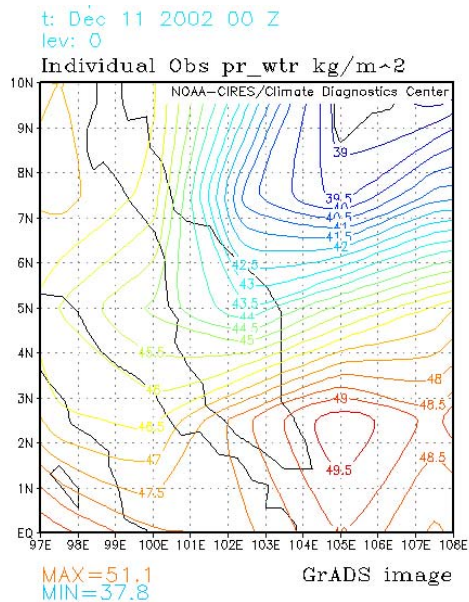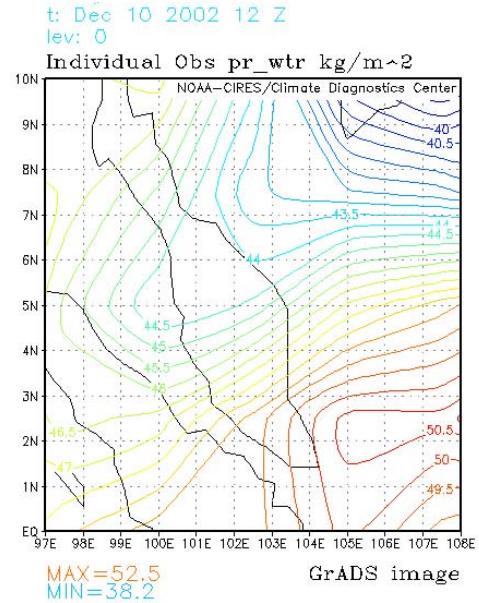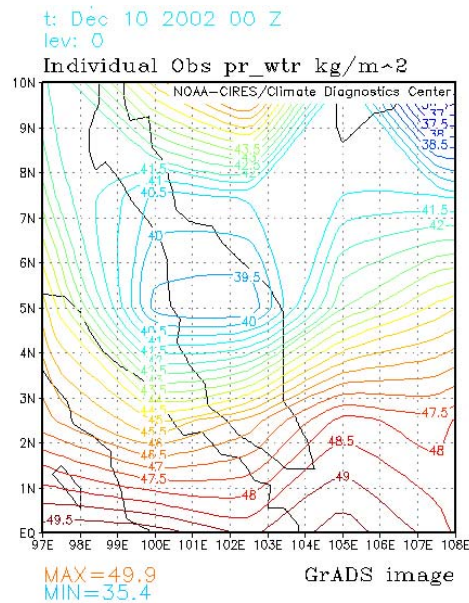
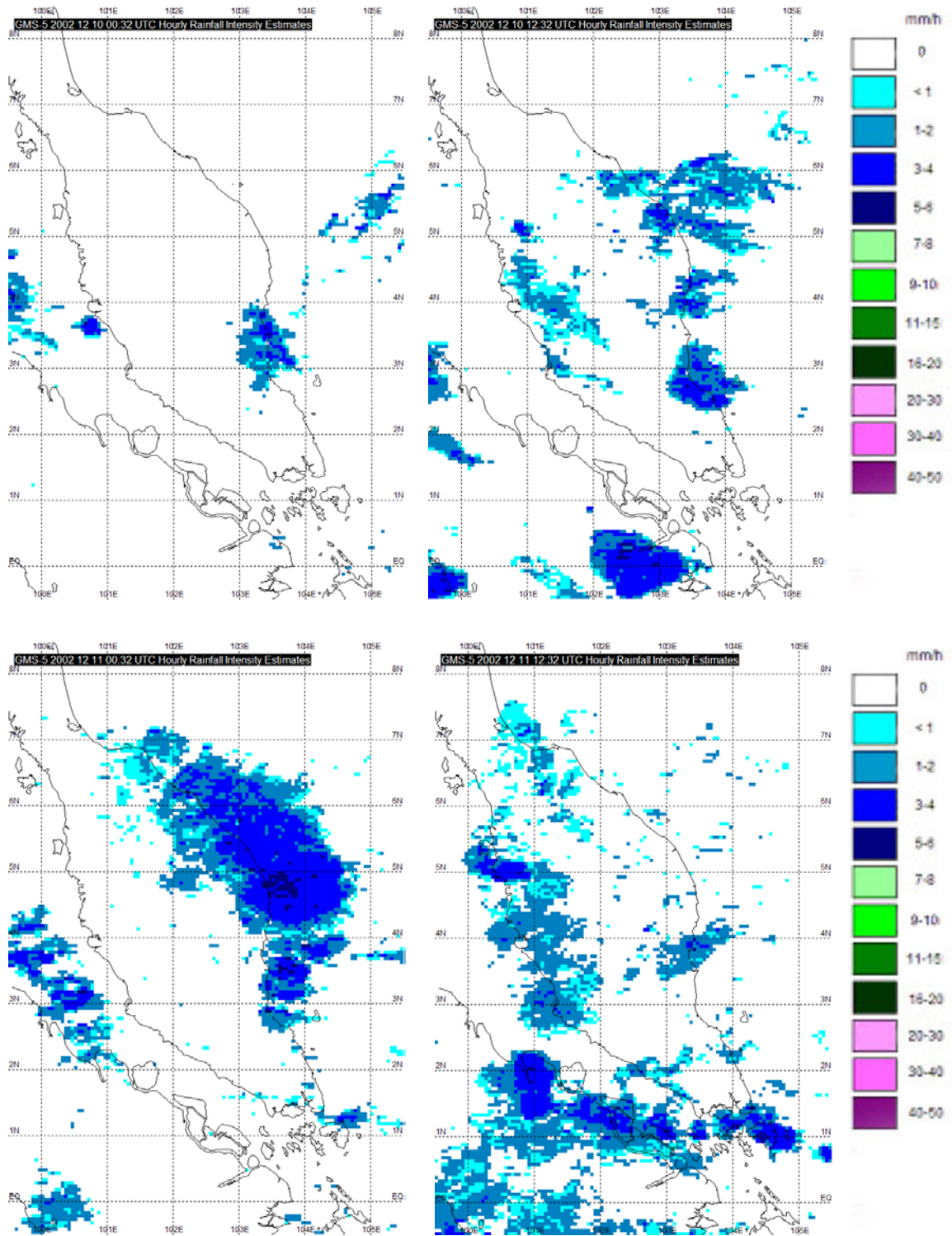Figure 5.6   As in Fig. 5.1 except for 10-11 December 2002.

Figure 5.7   As in Fig. 5.2 except for 10-11 December 2002.

5.2.2   Results and Discussion

From the following Fig. 5.8 and Fig. 5.9, on 10 December 2002, it can be seen that heavy rainfall was recorded at Kota Bharu, KT Airport and KT Climate stations starting from 1900Z and continued until 2300Z. The LUT seriously under estimates the rainfall amount and rates. The heaviest rainrate recorded at each station was 62.2, 43.4 and 47.6 mm/h respectively. This is the main reason why the LUT estimate seemed to lag behind in rainfall accumulation since the LUT estimate recorded a maximum of 9.5 mm/h of rainfall. While for Kuantan, the LUT estimate seemed to be slightly underestimating the rainfall until a heavy downpour of 25 mm/h occurred at 1900Z.

On 11 December 2002, heavy rainfall was recorded early at KT Airport, KT Climate and Kuantan and, to the lesser extent at Mersing starting from 0100Z to 0300Z with the heaviest rates recorded at each station being 28.8, 42.3, 17.4 and 14.6 mm/h respectively. The LUT estimate only gave a highest value of 9.5 mm/h at both KT Airport and KT Climate and a highest value of 5.5 mm/h for both Kuantan and Mersing. Generally a good improvement was shown by MWL, estimating cumulative rainfall fairly well for both KT Airport and Kuantan on 11 December 2002. While slightly over-estimating rainfall for both Kuantan on 10 December 2002 and Mersing on the next day, again the total rainfall for Mersing is quite small; it is only 41 mm. Although, MWL still underestimated the total rainfall for other stations, such as Kota Bharu, KT Airport and KT Climate on 10 December 2002 and KT Climate on the next day, the margin of errors had improved and these are the cases where rainfall is extremely heavy in a very

short time interval. Once again the temporal resolution of the observations makes it difficult to capture the most intense short rainfall bursts. Total rainfall for the day for all these stations exceeded 90 mm per day except for Kuantan and Mersing on 11 December 2002.
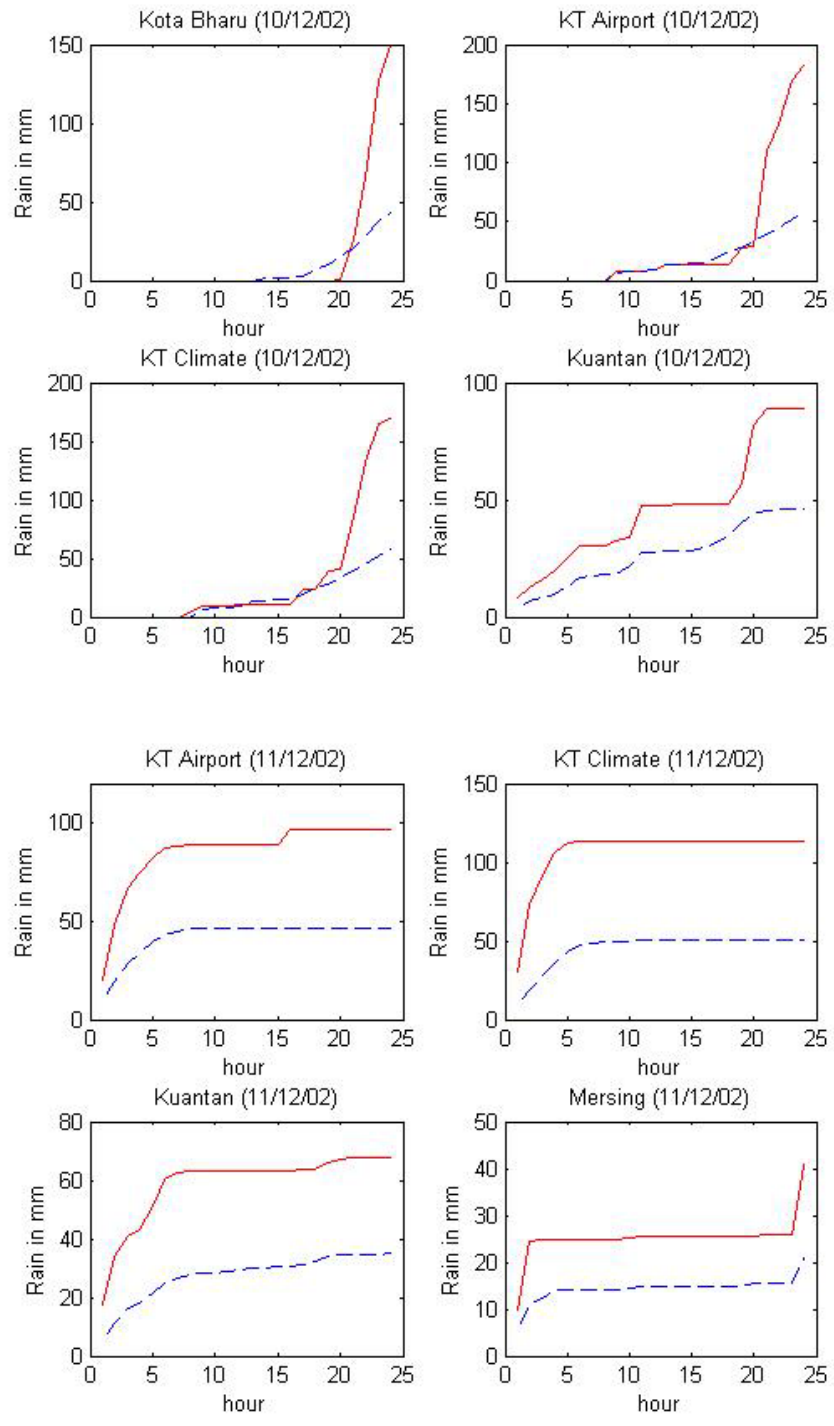
Figure 5.8   Cumulative rainfall for LUT (---) and RGV (—).

70
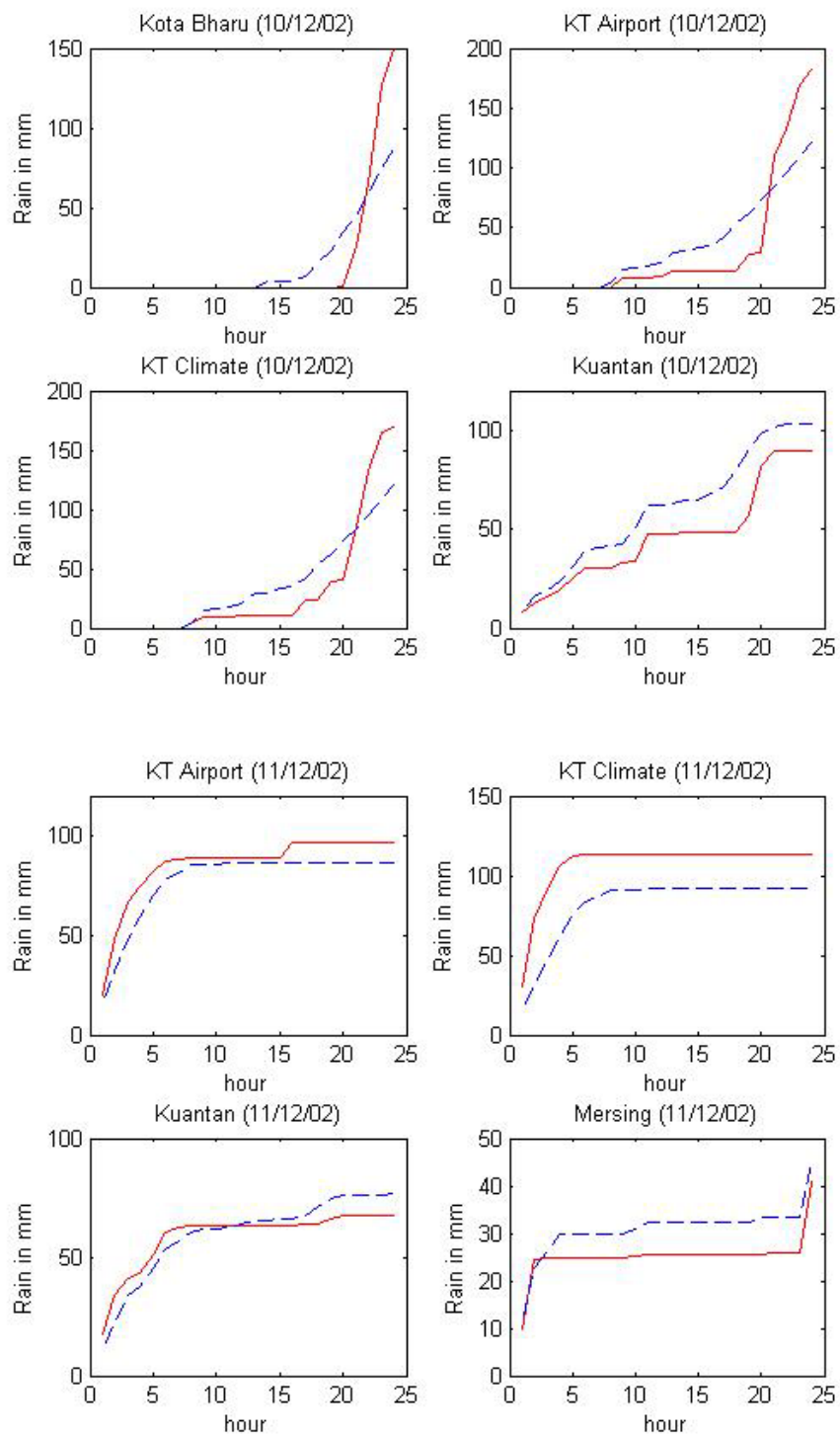
Figure 5.9   Cumulative rainfall for MWL (---) and RGV (—).

Using the hourly cumulative rainrate for this monsoon case, it can be seen that the LUT estimate always underestimated the rainfall when compared to RGV, while the MWL slightly underestimated the rainfall at the beginning but over-estimated at the end. Most of the times, the percentage error for MWL was below 30% except for a few occasions when it went above 30% error. For this case, the MWL estimate generally performed better than LUT as shown by the cumulative curves in Fig. 5.10 and the percentage errors in Table 5.2.
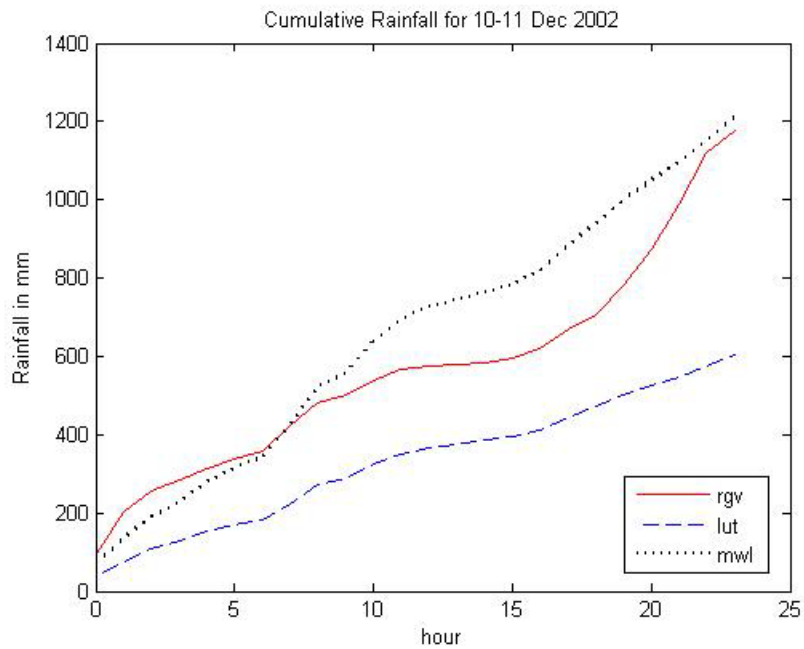
Figure 5.10   As in Fig. 5.5 except for 10-11 December 2002.

Table 5.2   Percentage error of LUT and MWL cumulative rainfall compared to RGV as in Fig. 5.10.

Time(Z)	00	01	02	03	04	05	06	07	08	09	10	11
LUT	57.4	62.3	57.8	55.2	51.7	49.6	48.7	46.7	43.8	42.6	39.2	38.1
MWL	25.2	33.3	25.6	19.8	12.1	6.9	3.8	0.7	8.3	10.9	18.8	22.2

Time(Z)	12	13	14	15	16	17	18	19	20	21	22	23
LUT	36.2	35.0	33.9	33.4	33.6	33.7	33.4	35.8	40.1	44.6	48.6	48.8
MWL	26.6	29.1	30.9	32.0	31.9	31.6	32.7	28.2	19.9	11.0	2.7	2.6

For case 2, the average percentage error for LUT is 43.8% and that of MWL is 19.5% and the difference between the two averages is quite large, which indicates that MWL estimate performed much better compared to LUT.

5.3　　8-9　December 2003 Case

5.3.1　　Event Overview

On 08 December 2003, a monsoon surge started affecting the center and southern regions of the east coast of Peninsular Malaysia. Heavy rainfalls were recorded over Kuantan and Mersing; at which the gauges read 193.6 and 203.8 mm respectively. Rain continued the following day, migrating slightly northward affecting the northern and central region of east coast. The rainfalls recorded over Kota Bharu, Kuala Krai and Kuantan were 104.2, 241.3 and 244.5 mm respectively on the following day.

The 12-h precipitable water analyses on 8 – 9 December 2003 is shown in Fig. 5.11 (http://www.cdc.noaa.gov/cdc/reanalysis/) and Fig. 5.12 shows the 12-h LUT rainfall estimate. The analyses showed the affected regions.

During this period, it was necessary to use GOES satellite data for our study because the GMS satellite data were not available any more. For this reason the slant angle is different from the previous two cases, since GOES was located at 155°E and GMS 140°E. The effect of the slant angle can be observed in Fig. 5.12.
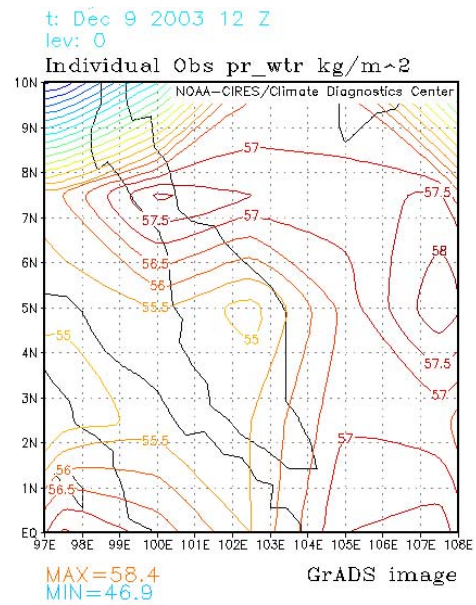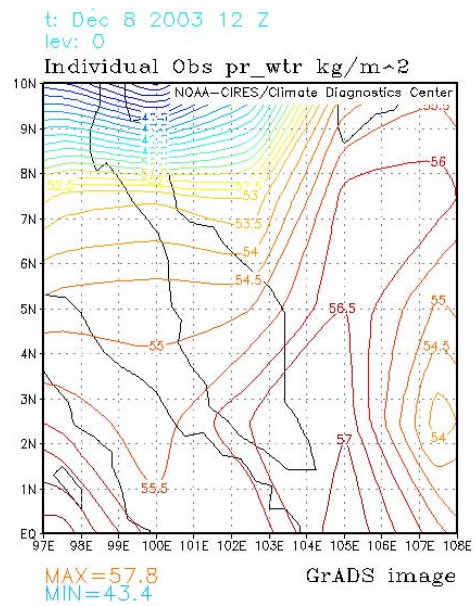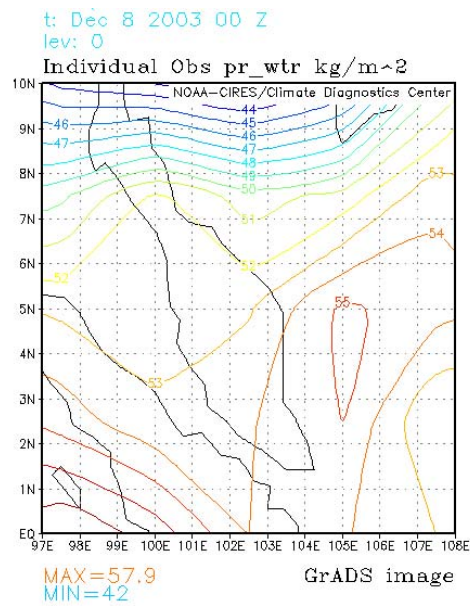
Figure 5.11   As in Fig. 5.1 except for 8-9 December 2003.

Figure 5.12   As in Fig. 5.2 except for 8-9 December 2003.

5.3.2   Results and Discussion

Again the LUT estimate shows quite good results for low cumulative rainfall rates below 20 mm/h, as is the case for Kuala Krai, Muadzam Shah, Kuantan and Mersing on 8 December 2003 and Kota Bharu, Kuala Krai and Batu Embun on the following day, but largely under-estimates the rainfall for Kuantan, which is due to the early hour heavy rainfall, as can be seen in Fig. 5.13. Kuantan recorded 40.0 mm/h at 0100Z and 62.5 mm/h at 0300Z while LUT only estimated 13.0 mm/h on both occasions. At larger cumulative values, LUT always under-estimates the rainfall and one can see a large difference between RGV and LUT in rainfall values. Kuantan and Mersing on 8 December 2003 show the effect of larger cumulative rainfall amounts and Kuala Krai and Kuantan on the following day show the effect of a large cumulative rainfall amount and heavy rainfall at short duration.

The MWL shows better estimates as compared to LUT; this can be seen in Fig. 5.14. The estimates are quite close to the RGV values with all the stations on 8 December 2003, including Kota Bharu and Kuala Krai the following day having a tendency to slightly over-estimate the amount. But for the case of Kuala Krai and Kuantan where the rainfall amount of the day was quite large with both stations recording over 200 mm, MWL shows some improvement, although still under-estimating the rainfall amount. For the case where rainfall amount is small, such as Batu Embun, which recorded only 41.8 mm, MWL tends to over-estimate the amount.
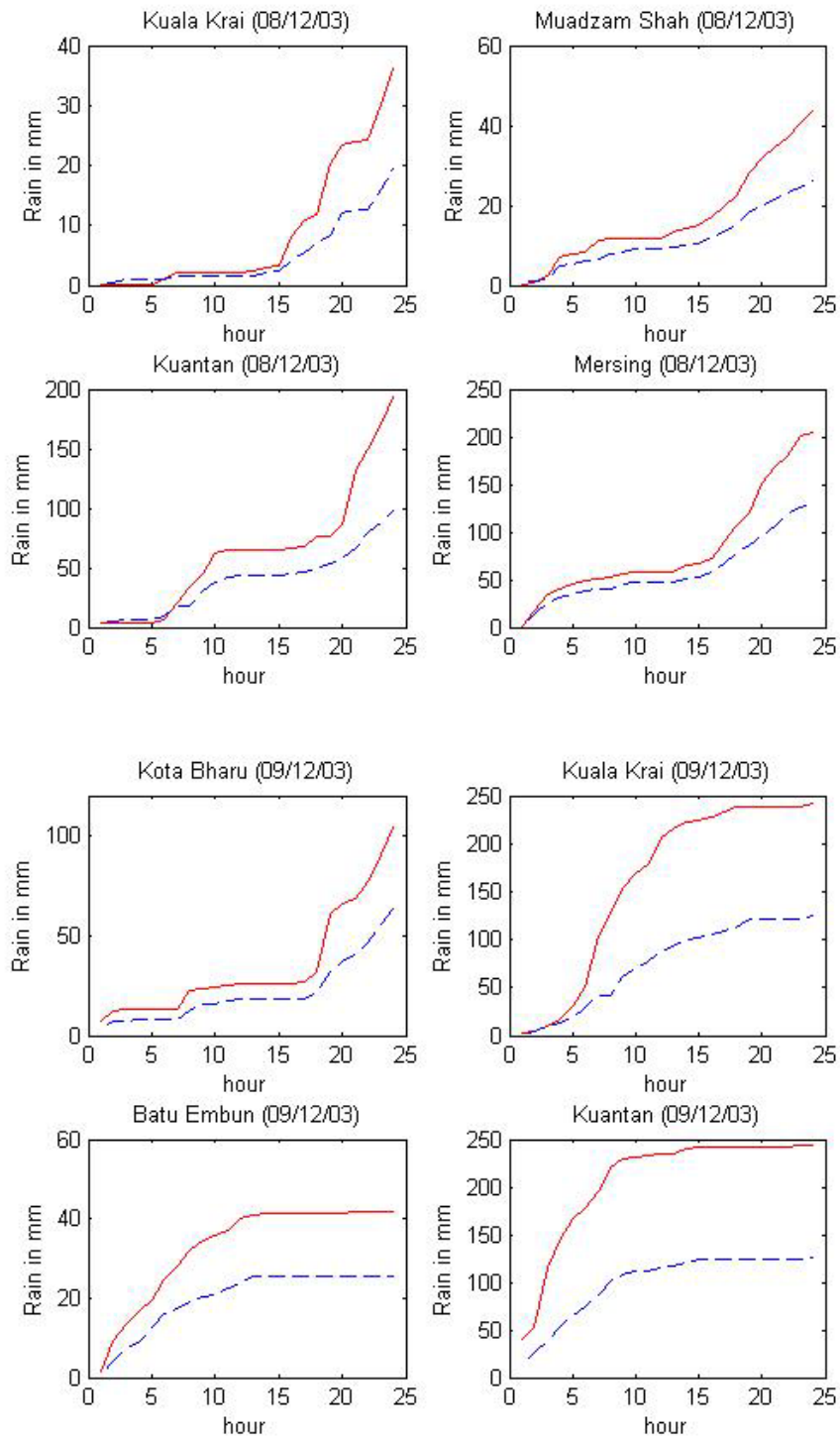
Figure 5.13   Cumulative rainfall for LUT (---) and RGV (—).
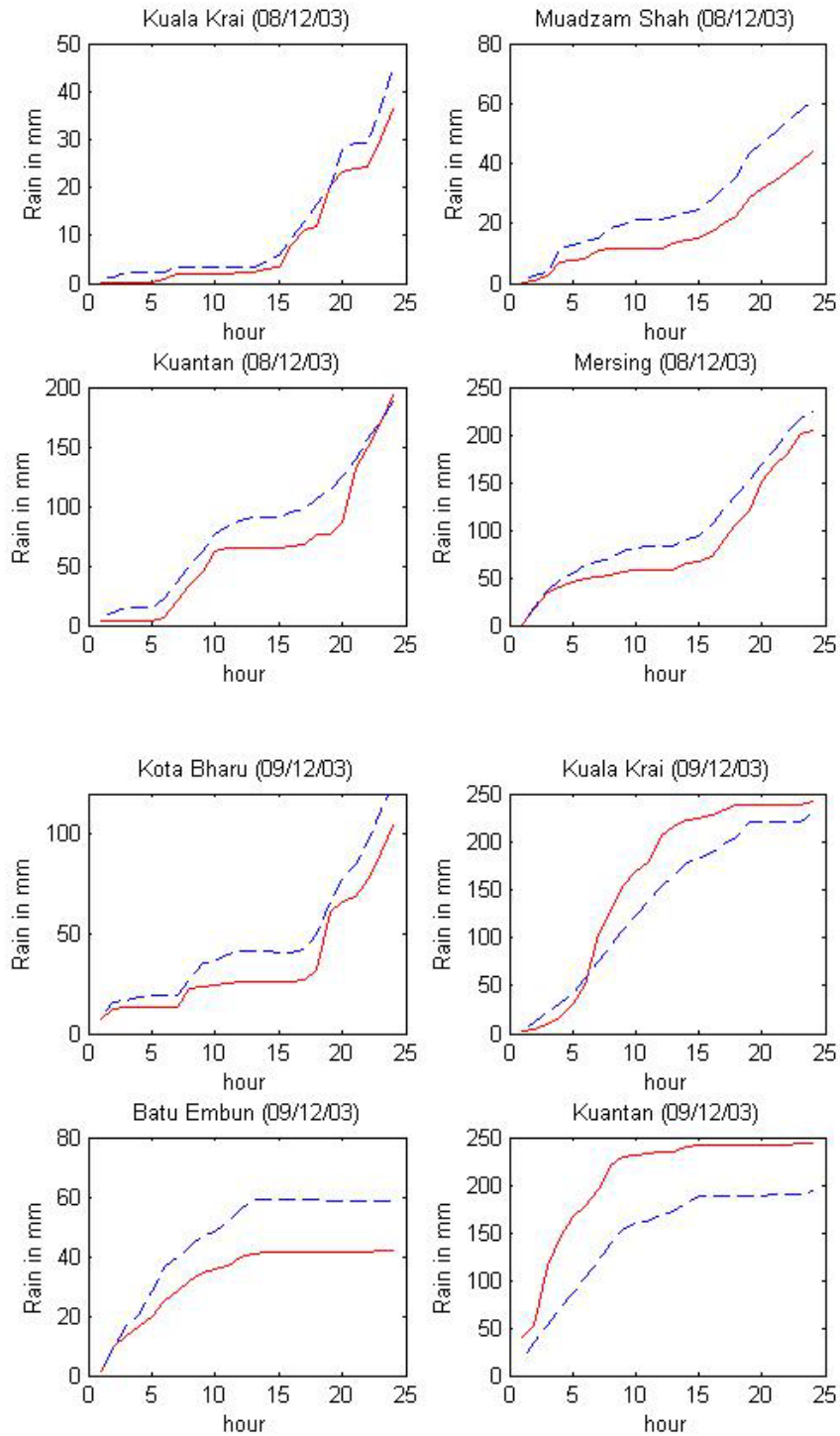
Figure 5.14   Cumulative rainfall for MWL (---) and RGV (---).

For this case study, generally, it can be seen that the LUT estimate consistently under-estimates the rainfall when compared to RGV, while the MWL consistently over-estimates the rainfall as shown by cumulative curves in Fig. 5.15. There was only a small difference in the percentage error for both LUT and MWL. The PE for LUT ranged from 11.0% to 23.6% while the PE for MWL ranged from 8.5% to 23.7%. The only marginal different was MWL estimates consistently returned smaller PE values as compared to LUT for at the last five hours toward the end of the day. Table 5.2 shows the PE for MWL and LUT estimates.
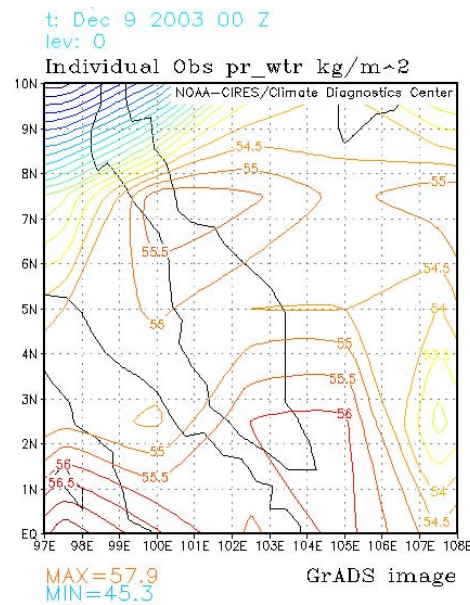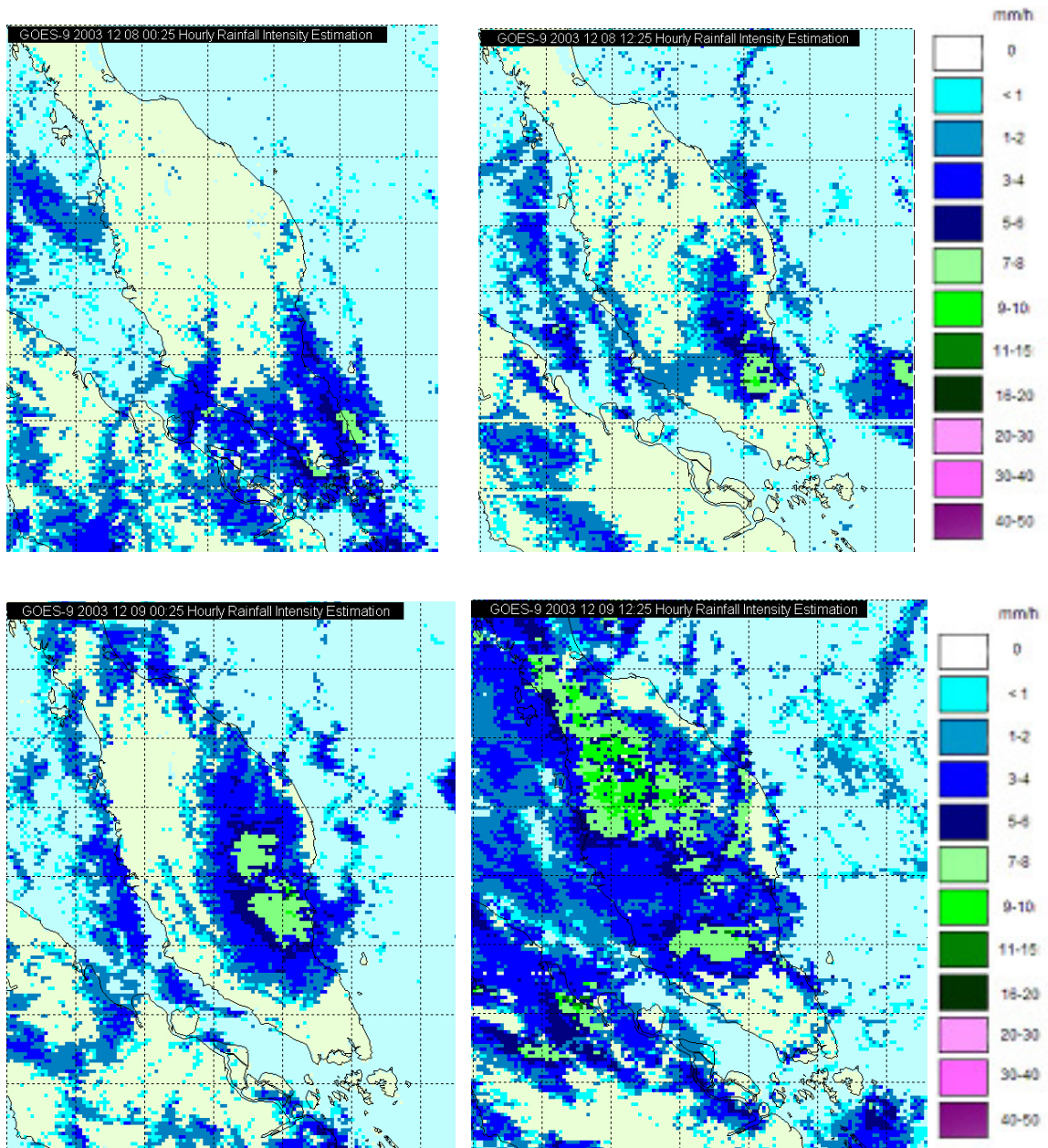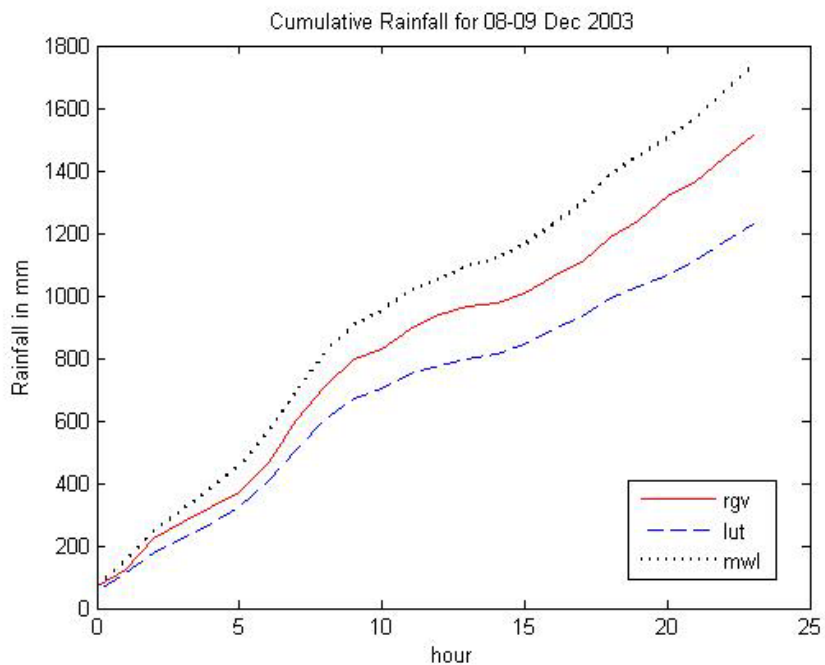

Figure 5.15   As in Fig. 5.5 except for 8-9 December 2003.

Table 5.3   Percentage error of LUT and MWL cumulative rainfall
compared to RGV as in Fig. 5.15

Time(Z)	00	01	02	03	04	05	06	07	08	09	10	11
LUT	23.6	11.0	20.9	18.1	15.9	12.7	12.7	15.8	14.4	15.7	15.3	16.1
MWL	3.0	23.4	8.5	13.7	17.4	23.7	20.8	14.7	15.8	13.8	15.0	13.8

Time(Z)	12	13	14	15	16	17	18	19	20	21	22	23
LUT	17.3	17.4	16.7	16.1	16.0	15.9	16.2	17.0	18.9	18.2	18.5	19.0
MWL	12.2	13.0	14.4	15.7	15.9	16.7	16.8	16.5	14.2	15.0	14.9	14.7

For case 3, the average percentage error for LUT is 16.6% and that of MWL is 15.2%, both the averages are relative small, which indicates that both MWL and LUT estimates performed quite well with MWL was marginally better.

5.4   Other Statistical Results

The statistical results of the three cases for comparison between LUT and MWL techniques are summarized in Table 5.4. The correlations of both LUT and MWL techniques with RGV are generally good, in the range of 0.70 to 0.81. For the storm case (case 1), the correlation is smaller than that of monsoon-type rainfall for both LUT and MWL. The biases for LUT are consistently negative which indicates under-estimation, while the biases for MWL are small positive values indicating slight over-estimation. The root mean square errors (RMSE) for MWL are generally smaller than that of the LUT in all the three cases. LUT shows a more evenly distributed pattern as indicated by its smaller standard deviation, suggesting that this technique does better for retrieving widespread and intensive rain events such as monsoon rain and storm type rain.

Table 5.4   Statistics of rainrate from RGV, LUT and MWL.

	RGV		LUT					MWL				
	Mean (mm/h)	SDev (mm/h)	Mean (mm/h)	SDev (mm/h)	RMSE (mm/h)	Bias (mm/h)	Corr	Mean (mm/h)	SDev (mm/h)	RMSE (mm/h)	Bias (mm/h)	Corr
Case1	1.11	3.96	0.83	1.54	3.09	-0.28	0.70	1.28	2.64	2.67	0.16	0.74
Case2	0.98	4.54	0.50	1.43	3.53	-0.48	0.81	1.01	2.76	2.99	0.03	0.78
Case3	1.26	4.69	1.02	2.21	3.36	-0.24	0.75	1.45	3.30	2.88	0.19	0.78

The least-squares best-fit regression lines for LUT and MWL against RGV were obtained from the scatter plots of daily rainfall for the entire study period as in Fig. 5.16. The regression lines for LUT and MWL against RGV is as equation (5.1) and equation (5.2) respectively.

$$LUT \quad = \quad 0.47* RGV + 7.3 \tag{5.1}$$

$$MWL \quad = \quad 0.86* RGV + 6.4 \tag{5.2}$$

The slope for MWL regression line is much greater than that of LUT, which is 0.86 as compared with 0.47. This indicates that MWL gave a better estimate as it slope value is closer to 1 as compared to LUT estimate. Residuals for both cases are quite large; 175.3 mm and 172.4 mm respectively. This indicates that the distributions of the rainfall values are quite dispersed and distributed away from the regression line.
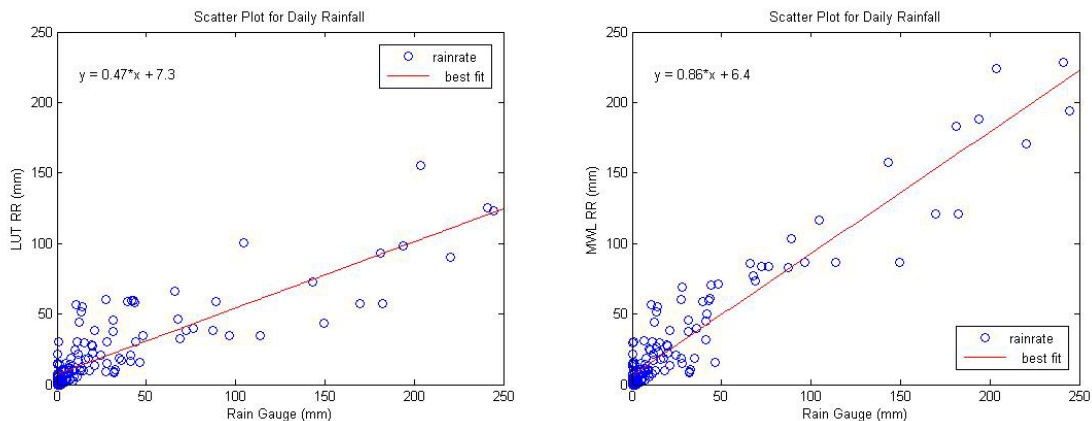
Figure 5.16   Regression lines for (a) LUT and RGV and (b) MWL and RGV

Another way to compare the performance of each technique is by deriving their rainrate using probability matching method as described in section 4.5.2. The PoR, mRR and RR for RGV, LUT and MWL were calculated for each of the cases as listed in Table 5.5. PoR values for LUT for all the cases is slightly larger than PoR for RGV, this means that LUT estimates pick-up rainfall more often than RGV. PoR values for MWL are the same as LUT since MWL is based on LUT estimate and only rainrate values of LUT are adjusted (i.e., when LUT value is zero so is MWL). This makes sense as one would expect it to be raining more frequently within the area of the pixel than at any particular point within that pixel.

The mRR values for LUT are generally smaller than that of the RGV; this means that most of the time the LUT estimate is returning smaller values than that of the RGV. The mRR for MWL has significantly smaller value than the mRR for RGV for case 2 and slightly larger values for case 1 and case 3. The difference in mRR values between MWL and RGV are smaller as compared to the difference in mRR values of LUT and RGV. This indicates the mean rainrate for MWL is closer to the rain gauge value compared to the mean rainrate for LUT.

The RR value is by far the most useful function; it indicates how well each technique performs as compared to RGV. The RR values for LUT are smaller than that of RGV for all three cases, indicating that the LUT tends to under- estimate the rainrate. The RR values for MWL are very close to RR values for RGV for case 1 and case 2. On both occasions it slightly over-estimates the rainrate. For case 3 the difference in RR between MWL and RGV

is slightly larger, and this is probably due to the slant of the look angle of the satellite coupled with the wind drift factor that might affect the value of RR for RGV. Table 5.5 below gives the values of the probability matching for each of the cases. Again this suggests a possible bias correction could be made.

Table 5.5   Probability matching values for RGV, LUT and MWL

	RGV			LUT			MWL		
Date	PoR	mRR	RR	PoR	mRR	RR	PoR	mRR	RR
Case 1	0.35	3.16	1.11	0.40	2.10	0.83	0.40	3.21	1.28
Case 2	0.15	6.77	0.98	0.20	2.55	0.50	0.20	5.10	1.01
Case 3	0.32	4.00	1.26	0.35	2.94	1.02	0.35	4.17	1.45

5.5 Summary

The results in the study indicate that for light rainfall of the order of 20 mm per day both LUT and MWL techniques give quite good estimates. However, there are instances where LUT and MWL tend to under-estimate the rainfall when there were heavy rainfalls that occurred in a very short time interval. Generally, the MWL gave a better estimate when rainfall amount is more than 20 mm although most of the time it tended to over-estimates the rainrate. The MWL tends to slightly over-estimate the rainrate when cumulative rainfall for the day was below 180 mm. Still, there are cases where MWL under-estimated the rainfall, especially where cumulative rainfall exceeded 180 mm or where intense rain of more than 30 mm per hour occurred.

The slope of the MWL regression line with the RGV is 0.86, which is closer to 1 as compared to the gradient of the LUT regression line, which is 0.47 suggesting that the MWL estimate performed better than the LUT estimate when compared to the RGV. The RR calculated from the probability matching method indicated that the RR values of MWL are much closer to the RR values of RGV as compared to the RR values of LUT.

Overall, it seems that the MWL performs much better than LUT. In particular, it avoids the severe under-estimation of heavy rainfall which can be a great problem in flood warning.

Chapter 6   Conclusions

6.1   Summary

Precipitation is one of the most difficult of all atmospheric variables to measure. No single standard of accuracy exists with which to assess new measurement methods. Rain gauge networks over populated continents provide, at best, poor sampling and are not always accurate, especially at times of strong winds. Over vast deserts and jungle areas, measurements are sparse while over the oceans they are virtually nonexistent. Pioneering efforts have been made to estimate rain from infrared and visible data of both polar-orbiting and geosynchronous metsats. The major cause of measurement error using these methods was the presence of high clouds, such as thick cirrus, which were not precipitating (Weng *et al*., 2003) and the physical restriction of retrieving rainfall information from observations of top of cloud.

The advanced microwave sounding unit has provided new tools for monitoring Earth's atmosphere due to its unique capability of penetrating through thin cirrus clouds and improving spatial and temporal resolutions as compared with the previous microwave instruments. In this study, we select a combination

of infrared and microwave techniques using the strength of each method to complement their deficiencies in trying to estimate monsoon rainfall over a tropical region. This passive microwave algorithm is the latest algorithm by NOAA NESDIS; it is highly correlated with the surface rain rates and is now directly used to monitor surface precipitation throughout the world (Weng *et al*., 2003).

6.2   Conclusion

In this study, we presented an attempt to combine the high temporal sampling by using Kurino's (1997) LUT technique, based on geostationary metsat IR brightness temperature, with the more physically direct but temporally sparse measurements of the NESDIS AMSU rainrate algorithm based on scattering processes. The NESDIS AMSU rainrate algorithm is the latest of many microwave techniques used in attempt to estimate the global rainfall. It appears promising for monitoring severe weather with heavy rainfall intensity as the derived parameter over tropical region, although more verification needs to be done using more densely distributed rain gauge networks and properly calibrated radar network in order to obtain a better result.

The MWL has, to a certain extent, demonstrated an ability to perform better than the LUT technique for heavier rainfall intensities. The results of this study are in good agreement with Ebert and Manton's (1998) finding that, for instantaneous rainfall, the IR, VIS/IR, AVHRR, and mixed algorithms had correlation coefficients ranging from 0.39 to 0.58, and SSM/I microwave algorithms performed much better than the IR-based algorithms with correlation coefficients in the range of 0.60 to 0.78. The result reaffirms that the microwave algorithms generally estimate instantaneous rain rates with much greater skill than do the more empirical algorithms that depend on infrared and visible data. It also demonstrates that the combined IR-based and microwave algorithm could provide a better estimation. In this study, we found that the correlation coefficients range from 0.70 to 0.81 as compared to rain gauge recording.

The main problem remains for MWL that it tends to under estimate rainfall when the daily rainfall exceeds 200 mm or when rainfall intensity exceeds 30 mm/h. This is primarily due to the nature of rainfall intensity over the tropics which are highly variable in time and space while the metsats observations are temporally sparse. Short duration (generally less than 1/2 hour) and small-scale features of weather over the tropics, especially near the equator; make the satellite rainfall estimates difficult and challenging. The temporal and spatial resolution of satellite observations are major factors affecting the accuracy of rainfall estimate. Beside that, the time lag between satellite-based observation and ground-based observation also has a significant impact on the results of the

study. But in such areas where rainfall originates over the ocean and moves over land, satellite methods are essential.

There remain several areas of improvement for satellite rainfall estimation. These include improved delineation of raining and non-raining areas, possible classification of rain into convective and stratiform types, improvements of the rain physics used by cloud models, infrared and microwave algorithms and further efforts to combine observations from different spectral regions and observing platforms. The newer passive microwave instruments with more channels (including polarization information) promise improvements also.

6.3   Future Directions

Future improvements to this satellite rainfall algorithm can be used in nowcasting applications as an early flood warning system. Property damages and loss of lives associated with the tropical monsoon rainfall sometimes are high. This then gives weather forecasters the ability to monitor location and magnitude of heavy monsoon rainfall more accurately and issue an early warning before the rainfall actually hits the coastal areas. In future, probably, it can be used for calibrating the radar over tropical regions, and as an input parameter for numerical weather forecasts such as mesoscale models.

On the global scale, the Global Precipitation Mission (GPM) project is planned to begin in 2008 as follow-on to the highly successful Tropical Rainfall Measuring Mission (TRMM) project and may provide 3-hourly sampling from PMW sensors. GPM precipitation products can be incorporated with the IR data from MTSAT and FY-2 to increase their resolution to 30 mins. These will greatly improve the temporal and spatial resolution of the future satellite-based rainfall estimates. The problem with time-lag between ground-based and satellite-based observation also will be greatly reduced.

Appendix A   Abbreviations

3D	Three-dimensional
AMSU	Advanced Microwave Sounding Unit
ASEAN	Association of Southeast Asia Nations
ASMC	ASEAN Specialized Meteorological Center
ATN	Advanced TIROS-N Spacecraft
AVHRR	Advanced Very High Resolution Radiometer
Corr	Correlation
CST	Convective-Stratiform Technique
DMSP	Defence Meteorological Satellite Program
DoD	Department of Defence
ESSA	Environmental Science Services Administration
EUMETSAT	European Organization Exploration Meteorological Satellites
FAR	False-Alarm Ratio
FY	Feng Yun
GATE	Global Atmospheric Tropical Experiment
GMS	Geostationary Meteorological Satellite
GOES	Geostationary Operational Environmental Satellite
GOMS	Geosynchronous Orbit for Meteorological Satellite

GPI	GOES Precipitation Index
GPM	Global Precipitation Mission
GCOM	Global Climate Observation Mission
GVAR	GOES Variable
INSAT	India National Satellite System
IR	Infrared
ITCZ	Intertropical Convergence Zone
ITOS	Improved TIROS Operational System
IWP	Ice Water Path
JMA	Japan Meteorological Agency
JTWC	Joint Typhoon Warning Center
LUT	Look Up Table
METEOSAT	European Geostationary Meteorological Satellite
METOP	EUMETSAT's Polar Satellite
METSAT	Meteorological Satellite
MMS	Malaysian Meteorological Service
mRR	Mean Rain Rate
MSG	Meteosat Second Generation
MTSAT	Multi-Functional Transport Satellite
MWL	Hybrid Microwave/Infrared Technique
NESDIS	National Environmental Satellite Data and Information Service
Nnr	Number of non-raining occurrences
NOAA	National Oceanic and Atmospheric Administration

NPOESS	National Polar Orbiting Environment Satellite System
Nr	Number of raining occurrences
NWP	Numerical Weather Prediction
PE	Percentage Error
PMW	Passive Microwave
POD	Probability of Detection
PoR	Probability of Rain
RGV	Rain Gauge Value
RMSE	Root Mean Square Error
RR	Rain Rate
SMS	Synchronous Meteorological Satellite
SSM/I	Special Sensor Microwave Imager
TIROS	Television and Infrared Observation Satellite
TRMM	Tropical Rainfall Measuring Mission
tRR	Total Rain Rate
VIS	Visible
VISSR	Visible and Infrared Spin Scan Radiometer
WMO	World Meteorological Organization

References

Ackerman, S. A., 1996: Global satellite observations of negative brightness temperature differences between 11 and 6.7 μm. *J. Atmos. Sci.,* **53**, 2803–2812.

Adler, R. F., and R. A. Mack, 1984: Thunderstorm cloud height-rainfall rate relations for use with satellite rainfall estimation techniques. *J. Climate Appl. Meteor*., **23**, 280-296.

Adler, R. F., and A. J. Negri, 1988: A satellite infrared technique to estimate tropical convective and stratiform rainfall. *J. Appl. Meteor.,* **27**, 30-51.

Arkin, P. A., 1979: The relationship between fractional coverage of high cloud and rainfall accumulations during GATE over the B-scale array. *Mon. Wea. Rev.,* **107**, 1382-1387.

Arkin, P. A., and B. Meisner, 1987: The relationship between large-scale convective rainfall and cold cloud over the Western Hemisphere during 1982-1984. *Mon. Wea. Rev.,* **115**, 51-74.

Bader, M. J., J. R. Grant, A. J. Waters and G. J. Forbes, 1995: *Images in Weather Forecasting: A Practical Guide for Interpreting Satellite and Radar Imagery*. Cambridge University Press, NY, 499 pp.

Barrett, E. C., 1970: The estimation of monthly rainfall from satellite data. *Mon. Wea. Rev.,* **98**, 322-327.

Barrett, E. C., 1973: Forecasting daily rainfall from satellite data. *Mon. Wea. Rev.,* **101**, 215-222.

Barrett, E. C., and D. W. Martin, 1981: *The Use of Satellite Data in Rainfall Monitoring*. Academic Press, NY, 340 pp.

Bennartz, R., A. Thoss, A. Dybbroe and D. B. Michelson, 2002: Precipitation Analysis Using the Advanced Microwave Sounding Unit In Support Of Nowcasting Applications. *Meteorological Appl.,* **9**, 177-189*.*

Chen, F. W., and D. H. Staelin, 2003: AIRS/AMSU/HSB Precipitation Estimates. *IEEE Trans. Geosci. Remote Sensing,* **41**, 410-417.

Conway, E. D., 1997: *An Introduction to Satellite Image Interpretation*. The Johns Hopkins University Press, MD, 242 pp.

Dittberner, G. J., and T. H. Vonder Haar, 1973: Large scale precipitation estimates using satellite data; application to the Indian Monsoon. *Arch. Met. Geoph. Biokl. Ser. B,* **21**, 317-334.

Ebert, E. E., and M. J. Manton, 1998: Performance of Satellite Rainfall Estimation Algorithms during TOGA COARE. *J. Atmos. Sci.,* **55**, 1537-1557.

Ferraro, R. R., F. Weng, N. C. Grody, L. Zhao, H. Meng, C. Kongoli, P. Pellegrino, S. Qiu, and C. Dean, 2005: NOAA Operational Hydrological Products Derived from the Advanced Microwave Sounding Unit. *IEEE Trans. Geosci. Remote Sensing,* **43**, 1036-1049.

Goodrum, G., K. B Kidwell, and W. Winston, 2001: *NOAA KLM User's Guide*. U.S. DoC, NOAA, NESDIS, NCDC, Suitland, MD, Sec 3.3.

Griffith, C. G., W. L. Woodley, J. S. Griffin, and S. C. Stromatt, 1980: *Satellite-Derived Precipitation Atlas for the GARP Atlantic Tropical Experiment.* Division of Public Documents, U.S. Government Printing Office, Washington DC, 284 pp.

Grose, A. M. E., E. A. Smith, H. S. Chung, M. L. Ou, B. J. Sohn, and F. J. Turk, 2002: Possibilities and limitations for QPF using nowcasting methods with infrared geosynchronous satellite imagery. *J. Appl. Meteor.,* **41**, 736-785.

Inoue, T 1987: A cloud type classification with NOAA 7 split window measurements. *J. Geophys Res.*, **92**, 3991-4000.

Kidder, S. Q., and T. H. Vonder Haar, 1995: *Satellite Meteorology: An Introduction*. Academic Press, CA, 466 pp.

Kummerow, C., Y. Hong, W. S. Olson, R. F. Adler, J. McCollum, R. Ferraro, G. Petty, D. B. Shin, and T. T. Wilheit, 2001: The Evolution of the Goddard Profiling Algorithm (GPROF) for Rainfall Estimation from Passive Microwave Sensors. *J. Appl. Meteor.,* **40**, 1801-1820*.*

Kurino, T., 1997: Rainfall Estimation with the GMS-5 Infrared Split-Window and Water Vapor Measurement. *Meteorological Satellite Center Technical, JMA, Note No.* **33**, 91-101.

Lovejoy, S., and G. L. Austin, 1979: The source of error in rain amount estimating schemes for GEOS visible and IR satellite data. *Mon. Wea. Rev.,* **107**, 1048-1054.

Lovejoy, S., and G. L. Austin, 1980: The estimation of rain from satellite-borne microwave radiometers. *Q. J. Roy. Meteor. Soc.,* **106**, 255-276.

Moten, S., 2003: The Tropical Storm Vamei. *25th Meeting of Asean Sub-Committee on Meteorology and Geophysics (SCMG),* Petaling Jaya, Malaysia.

Negri, A. J., R. F. Adler, and P. J. Wetzel, 1984: Rain Estimation from Satellites: An Examination of the Griffith-Woodley Technique. *J. Climate Appl. Meteor*., **23**, 102-116.

Oh, H. J., B. J. Shon, E. A. Smith, F. J. Turk, A. S. Seo, and H. S. Chung, 2002: Validating Infrared-based Rainfall Retrieval Algorithms with 1-minute Spatially Dense Raingage Measurement over Korean Peninsula. *Meteor. Atmos. Phys*., **81**, 273-287.

Petty, G. W., 2004: *A first Course in Atmospheric Radiation*, Sundog Publishing, WI, 444 pp.

Rao, P. K., S. J. Holmes, R. K. Anderson, J. S. Winston, and P. E. Lehr, 1990: *Weather Satellites: Systems, Data, and Environmental Applications*. American Meteorological Society, MA, 503 pp.

Scofield, R. A., and V. J. Oliver, 1977: *A Scheme for Estimating Convective Rainfall from Satellite Imagery*. NOAA Tech. Memo. NESS 86, DC, 47 pp.

Smith, E. A., A. Mugnai, H. J. Cooper, G. J. Tripoli, and X. Xiang, 1992: Foundations for statistical-physical precipitation retrieval from passive microwave satellite measurements. Part I: Brightness-temperature properties of a time- dependent cloud-radiation model. *J. Appl. Meteor.,* **31**, 506-531.

Spencer, R. W., 1986: A satellite passive 37-GHz scattering-based method for measuring oceanic rain rates. *J. Climate Appl. Meteor*., **25**, 754-766.

Spencer, R. W., H. M. Goodman, and R. E. Hood, 1989: Precipitation retrieval over land and ocean with SSM/I: Identification and characteristics of the scattering signal. *J. Atmos. Ocean Tech.,* **6**, 254-273

Staelin, D. H., and F. W. Chen, 2000: Precipitation Observations Near 54 and 183 GHz Using the NOAA-15 Satellite. *IEEE Trans. Geosci. Remote Sensing,* **38**, 2322-2332.

Stout, J. E., D. W. Martin, and D. N. Sikdar, 1979: Estimating GATE rainfall with geosynchronous satellite images. *Mon. Wea. Rev.,* **107**, 585-598.

Tsonis, A. A., and G. A. Isaac, 1985: A new approach for instantaneous rain area delineation in midlatitude using GOES data. *J. Climate Appl. Meteor*., **23**, 1393-1410.

Vicente, G. A., R. A. Scofield, and W. P. Menzel, 1998: The operational GOES infrared rainfall estimation technique. *Bull. Amer. Meteor Soc.,* **79**, 1883-1898.

Wallace, J. M., and P. V. Hobbs, 1977: *Atmospheric Science: An Introductory Survey.* Academic Press, NY, 350 pp.

Weng, F., L. Zhao, G. Poe, R. R. Ferraro, X. Li, and N. C. Grody, 2003: AMSU cloud and precipitation algorithms. *Radio Sci*., **38**, 8068-8079.

Wilks, D. S., 1995: *Statistical Methods in the Atmospheric Sciences: An Introduction.* Academic Press, CA, 467 pp.

Zhao, L., and F. Weng, 2002: Retrieval of ice cloud parameters using the advanced microwave sounding unit (AMSU). *J. Appl. Meteor.,* **41**, 384-395.